Montanuniversitat Leoben

Influence of Al on structure and mechanical properties of YN and HfN

Leoben, June 2011

This thesis was supported by the Austrian Science Fund through the project FWF-Start-Project Nr. Y371.

Affidavit:

I declare in lieu of oath, that I wrote this thesis and performed the associated research by myself, using only literature cited in this volume.

Leoben, June 2011

Acknowledgements

First of all, I want to express my gratitude to **Assoc.Prof.Dr. Paul Mayrhofer,** giving me the possibility and necessary support in writing this thesis.

I would like to give my sincere gratitude to **DI. Richard Rachbauer,** my supervisor who, with his extraordinary patience and consistent encouragement, gave me great help by providing me with necessary materials, advice of great value and inspiration of new ideas. It is his suggestions that draw my attention to a number of deficiencies and make many things clearer. Without his strong support, this thesis could not have been the present form.

Furthermore, my heartfelt thanks also goes to all members of the **Department of Physical Metallurgy and Materials Testing** for their help with this thesis. I would like to thank especially **Gerhard Hawranek.**

I owe many thanks to my beloved husband **Zehua Zhang,** for helping me get through the difficult times, and for all the emotional and life support. I owe many thanks to my cute daughter **Olivia Zhang,** who brings joy to my life.

I want to thank also all my friends for their support and friendship.

Finally, and most importantly, I wish to thank **my parents.** They bore me, raised me, supported me, taught me, and loved me. To them I dedicate this thesis.

Table of contents

List of figures

List of tables

1 Introduction

Nowadays, the shortages of resources make the researches for materials, which have excellent wear and corrosion resistance, imperative. One of the more effective means of reducing damage due to corrosion and wear is by sophisticated surface engineering, which means a specific surface treatment of a functional component in a way that it can perform functions that are quite distinct from those usually obtained from the bulk properties of the material. Surface engineering thus incorporates all the techniques which include both coating and modification of the surface by e.g. ion implantation or laser beam melting [1-2].

In fact, thin films have been applied in various application fields such as electronic and optical devices or protective hard coatings for more than half a century. Until today, thin film technology is a continually developing and growing field of science, as it moreover allows for the development of materials with precisely defined nanostructure and application tailored properties [3].

Transition metal nitrides (TMN) are thereby acknowledged as industrially standard coating materials for several decades in order to increase the hardness and prolong the lifetime of cutting tools [4]. Applied in severe working environments, these coatings are required not only due to their high hardness and wear resistance, but also because of their good oxidation and excellent corrosion resistance. Higher machining speeds and environmentally friendly technologies, minimizing the coolant-flow, thus imply higher cutting temperatures and therefore require superior oxidation resistant materials [5]. For example, TiN_z films exhibit high hardness and good wear resistance. However, when the temperature of the working environment is increased above 550 ^{o}C, TiN_z oxidizes to form rutile-structure TiO_2, whose porous morphology enables for rapid growth of the oxide scale [6]. For this reason, complex multicomponent nitrides have entered the field of application [7]. For instance, Ti-Al-N is a very popular coating for high-speed cutting manufacturing processes, due to its better hot hardness and oxidation performance. With incorporation of Al in TiN_z the presence of a protective Al_2O_3 layer is formed at high temperatures [5]. Therefore, the oxidation resistance of Ti-Al-N coatings is increased. At the same time, it has been found that the alloying of TiN with AlN promotes the cutting performance of the coating due to age-hardening mechanisms [8]. With increasing Al-content (x~0.6-0.7) a structural transition from cubic (B1, NaCl-prototype) to a mixed structure of cubic and hexagonal (B4, ZnS-wurtzite-prototype) occurs. A further increase of the Al content (x>0.74) results in a single phase wurtzite structure [9]. Both mechanical and thermal stability strongly scale with the Al content in the single phase cubic regime [10].

Further, TMN are widely used in various other fields because they combine this high mechanical strength, chemical inertness, and high thermal stability with often remarkable

optical and electronic properties. Especially, the growth of thin films with defined electronic properties, which can be adjusted in the range from metallic to insulating conduction behavior, allows for a huge application regime in the field of microelectronics [11].

Some TMN such as ScN_z, YN_z, GdN_z and LaN_z are indirect semiconductors with band gap energies of ~ 1-2 eV [12]. Among these transition metal nitrides, Yttrium nitride is also predicted to exhibit a high Mn solubility, which could imply good magnetic properties while retaining its semiconductor properties [13]. Further YN_z exhibits a very high melting point and a high elastic modulus [11].

In this thesis, YN_z, Y-Al-N and Hf-Al-N coatings are deposited on silicon substrate by unbalanced magnetron sputtering using N2 as reactive gas and Ar as working gas. The synthesized coatings are characterized by X-ray diffraction (XRD), scanning electron microscopy (SEM), the ball crater technique (Calo®-test) and nanoindentation, in order to investigate the oxidation behavior and mechanical properties of the film. Both ternary systems ($Y_{1-x}Al_xN$ and $Hf_{1-x}Al_xN$) are obtained by incorporation of Al in the fcc-YN and the fcc-HfN. The structural transition from a single phase cubic towards a single phase wurtzite structure is investigated as a function of the increasing Al content and shown to strongly influence the discussed mechanical and oxidation properties of the thin films.

2 Deposition fundamentals

2.1 General

Thin film technology is simultaneously one of the oldest arts and one of the newest sciences. With the development of technology, diverse fields of applications arise for thin films, such as e.g. electronics, optics, space science, aircrafts, defence and other industrial purposes. Thereby, thin films are deposited onto bulk materials (substrates) to achieve properties unattainable or not easily attainable in the single substrates [14]. Especially, the effect of size, stemming for film thicknesses in the order of several microns down to just a few atomic layers [15] allows for completely different properties compared to bulk materials. The combination with specific microstructures in thin films further enhances the applicability of thin films in terms of application tailored materials design [16]. Since, the properties of thin films are often influenced by the properties of the underlying material, the thickness and deposition conditions of the film become crucial for the final film properties [15].

Thin film deposition processes are commonly classified in four general categories:

- Physical vapor deposition (PVD): E.g., Evaporation, Sputtering, Ion plating.
- Chemical vapor deposition (CVD): E.g., Thermal, Plasma activated, Photon activated, Laser induced.
- Electrochemical deposition: E.g., Cathodic deposition, Anodic oxidation.
- Chemical deposition: E.g., Electroless.

All of these methods have their benefits and drawbacks. For this reason they are applied to suitable fields to create coatings with optimal properties, without changing the substrate properties negatively [17]. PVD and CVD are nowadays the main methods for fabricating thin films, thereby implementing the gas phase to transport/deposit coating material as discussed below [16-17].

There are three steps in the formation of a deposit: [18]

- Synthesis or creation of the depositing species.
- Transport from source to substrate.
- Deposition onto the substrate and film growth.

In a given process the versatility or flexibility is determined by the degree of independent control of these three steps. These three steps can be individually controlled in a PVD process, where a great flexibility in controlling the structure, properties, and deposition rate plays an important role. There are two major differences between CVD and PVD, which are mainly related to the creation of the deposited material and the temperature regime necessary. The major component like the metal vapor of the coating material within a PVD process is generated by a physical process, whereas within a CVD process also the metal vapor is generated by a chemical process. The PVD process can be carried out at comparatively low bulk substrate temperatures (i.e. < 500 ^{o}C). Thus materials such as hardened high speed steel and hot working tool steels can be coated with ceramic films without being softened. The CVD process needs much higher substrate temperatures of about 800-900 ^{o}C, whereby the process has only found widespread usage on materials which can withstand such a temperature without softening or appreciable distortion. Therefore, this technique is limited to thermally stable materials [19].

2.2 The PVD process

The PVD method covers a number of coating techniques, all of them characterized by a transfer process of the material from a solid phase into a vapor phase at low pressure and the condensation of the vapor as a thin solid film on a substrate. Typically, films using PVD processes can reach thicknesses, in the range of a few nanometers to thousands of nanometers. Moreover, PVD processes can be used to deposit single thin film layers as well as composition gradient layers, or multilayer coatings. The PVD can be divided in three main process variants: evaporation, ion plating, and sputtering [20-21].

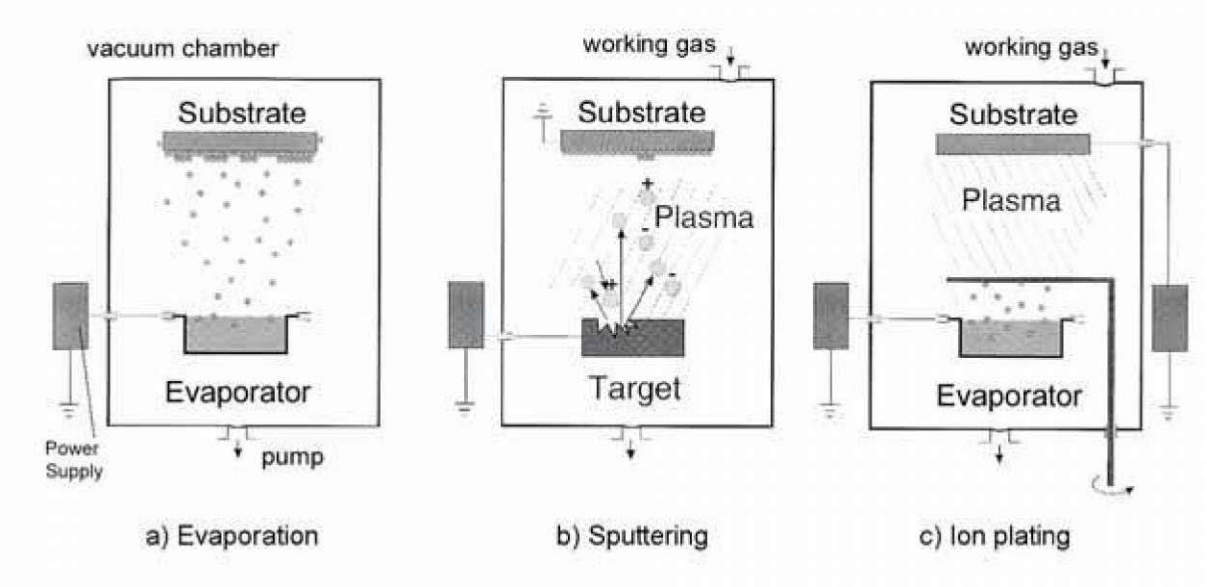

Fig. 2.1: Basic variations of PVD processes [16].

Evaporation

Evaporation, as shown in Fig. 2.1a, is arguably the simplest deposition method. The evaporation process is accomplished in a high-vacuum chamber in which the desired material is vaporized by heating either by direct resistance, radiation, eddy current, electron beam, laser beam, or an arc discharge. The typical pressure range of evaporation is 10^{-5} to 10^{-6} mbar. The evaporated atoms then travel towards the substrate and the walls of the chamber at high velocity in straight-line trajectories to be deposited there. The concentration of the growth species in the gas phase can easily be controlled by varying the source temperature [20-24].

Sputtering

In a sputtering process (Fig. 2.1b) the charged particles, originating from a plasma, are accelerated towards the target surface (coating materials). The accelerated particles transferring their momentum to the target surface atoms leading to atomic collision cascades within the target material. In this way one or more target atoms can be ejected and then travel to the substrate. A threshold energy that must be higher than the surface binding energy of the target atoms is required for sputtering [25-26].

Ion plating

Ion plating is a hybrid process in which the coating material is vaporized by thermal energy or momentum transfer in an anodic source. The vaporized atoms are ionized by a discharge after leaving the source. A high negative bias voltage applied at the substrate creates the ionizing plasma discharge at low pressure and accelerates the resulting ions to the substrate. The substrate and growing film are continually subjected to bombardment with energetic particles

prior to and/or during the deposition process leading to improved adhesion and modified film properties [27-29].

2.3 Plasma

A plasma which is referred to as the fourth state of matter, is required in the sputtering process as well as in ion plating. In general, a plasma consists of a mixture of electrons, ions, and neutral species. Although there are free electric charges in a plasma, a plasma is electrically neutral on the whole, due to the balance of positive and negative charges per volume. Thus, it can be defined as a quasi neutral gas of charged and neutral particles characterized by a collective behavior. In the plasma process, the gas is highly energized, therefore its electrons break free from their nucleus [16, 30-31].

2.3.1 DC glow discharge

A plasma may be generated by voltage in either direct current (DC) mode or at alternating current mode at e.g. radio frequency (RF), or microwave (MW) applied to a gas. A DC glow discharge can be obtained in a gas atmosphere by applying a voltage between both conductive electrodes at low pressure. As the electrical field is increased with applied voltage, available free electrons are accelerated, thereby increasing their kinetic energy. These fast electrons lose energy in collisions with the heavy neutral gas particles, which thereby become ionized. This continuous process is called the glow discharge phenomenon, see Fig. 2.2.

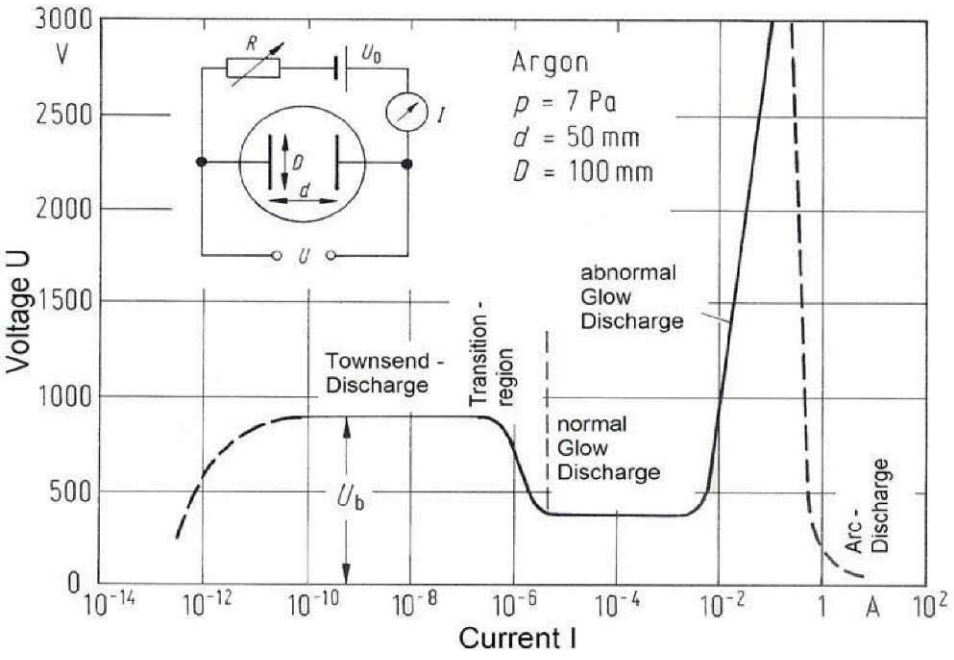

Fig. 2.2: Current-voltage characteristics in a glow discharge [32].

At first a very small current flow is produced, due to the existence of the few ionized particles which can contribute to the current. Increase of the voltage leads to the creation of more charged particles by impact ionization. By charge multiplication, the current increases steadily, the voltage thereby remaining constant, limited by the high output impedance of the voltage supply. This range of the discharge is frequently called a Townsend discharge.

With increasing voltage, an avalanche process takes place. Ions are accelerated in the field towards the cathode, strike the cathode and secondary electrons are produced. At the same time, new ions are produced, because of the electron collisions with the residual gas atoms and molecules. When enough of the electrons generated, producing sufficient ions to regenerate the same number of initial electrons, the discharge becomes self-sustaining. At this point, the plasma begins to glow, the current rises abruptly, and the voltage drops. The mode of the discharge at this point is called normal glow.

In this region, the cathode is bombarded unevenly, as the ion bombardment is focused near the edges of the cathode or at other surface irregularities. As the power is increased, the current raises sequentially, leading to a spread of the discharge over the whole cathode surface until a nearly uniform current density is achieved. Higher currents result in an abnormal discharge stage which is normally applied in a sputtering process. The sputtering process will be elaborated in detail in the following section.

A further increase in current results in the formation of spontaneous arc discharges. This stage exhibits very high currents and ionization rates. This regime is used for the cathodic arc evaporation process [32-35].

2.4 Sputtering

Sputtering is performed in a vacuum chamber, using energetic ions (commonly argon ions) from the plasma to knock atoms or molecules out from a target that acts as the cathode, which are subsequently deposited on a substrate (anode) by condensation. There are several different sputtering configurations that are used to deposit thin films for various substrates and materials to be deposited. The simplest and most widely used configuration is the planar arrangement, in which two planar electrodes are placed opposite each other. There are many variations, where DC, RF, magnetron and reactive sputtering will shortly be described in the following chapters.

2.4.1 DC sputtering

The DC sputtering system is the simplest model of the sputtering systems. Thereby, a DC power supply creates a high voltage between a pair of planar electrodes. The target material to be deposited serves as the cathode which is kept at a constant negative potential. DC sputtering has two basic requirements, one is the source material must be electrically conductive and the other is that the source material must have the ability to emit electrons. On the opposite side of the cathode is the anode, with the substrates placed on it, and/or the vacuum chamber walls may act as an anode. Both of the electrodes are separated typically a few centimeters. In the DC sputtering process the vacuum chamber is filled with an inert gas, typically Argon gas at ~10 Pa. The plasma is created and sustained by the DC source via mechanisms that pertain to the abnormal glow regime, involving secondary electron emission at the cathode and impact ionization of neutral gas atoms. Fig. 2.3 shows a typical DC sputtering configuration [36-38].

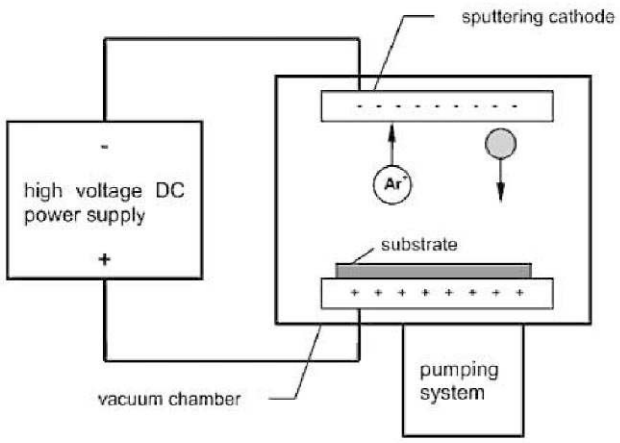

Fig. 2.3: A typical DC sputtering configuration [37].

2.4.2 RF sputtering

Radio frequency (RF) sputtering essentially works due to the target self-bias to a negative potential. The polarization of the target is reversed so as to attract, alternatively, the positive ions bombardment of atoms for subsequent deposition and the electrons which neutralize the positive surface charge. Compared to the DC sputtering, one major difference is that RF sputtering requires impedance matching between power supply and discharge chamber [1, 39]. This technique gains great importance for target materials with low electrical conductivity, or to enable sputtering of materials that form insulating top layers during sputtering in a reactive atmosphere, as explained below.

2.4.3 Magnetron sputtering

For the sake of high deposition rates the magnetron sputtering was developed on the basis of the conventional sputtering processes. In magnetron sputtering a magnet is positioned behind the target. The magnetic fields act in concert with the cathode surface to form electron traps. This electron trapping effect increases the collision rate between electrons and sputtering gas molecules. In other words, the magnetic field increases the ionization near the target, i.e increase of the current density at the cathode target, thus increasing the sputtering rate. On the other hand, the target-generated secondary electrons do not hit the substrates, and thus do not increase the substrate temperature. In magnetron sputtering, erosion of the target is local due to the cycloidal motion of electrons, which lowers the utilization rate of the target [37, 40].

There are two types of the magnetron sputtering: conventional balanced magnetron (CBM) and the unbalanced magnetron sputtering (UBM), as shown in Fig. 2.4. The difference between both processes is the distribution of the magnetic field. In CBM the magnetic field lines have the shape of a closed circuit, meaning that most of the field lines that exit the surface at one pole reenter the surface at the other pole. Therefore, the majority of electrons are trapped near the target to enhance the discharge, and only few electrons of the plasma will reach the substrate and bombard it. This will give only some substrate heating and bombardment during growth, which can modify the thin film structure. This issue can effectively be realized using an unbalanced magnetron configuration (Fig. 2.4b), where magnets with different magnetic properties are used, leading to the formation of an open magnetic field. Hence electrons can reach further outward, along the magnetic field lines, which results in broadening of the plasma from the target to substrate. Under these conditions thin films can also be bombarded during deposition with charged particles, and the surface diffusion can be promoted during film growth. Therefore, the thin film structure can be effectively modified in an unbalanced magnetron sputtering process [41-43].

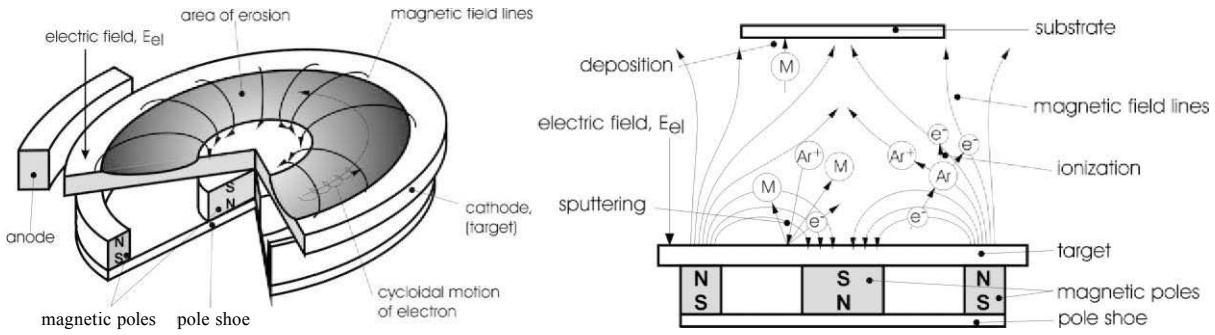

(a) (b)

Fig. 2.4: Balanced magnetron configuration (a) and unbalanced magnetron configuration (b) [44].

2.4.4 Reactive sputtering

In reactive sputtering, the deposited film is formed by a chemical reaction between vaporized target material and a reactive gas, such as nitrogen and oxygen, which is introduced into the vacuum chamber. Oxide and nitride films are often fabricated using reactive sputtering. The composition of the film can be controlled by varying the relative pressures of the inert and reactive gases [45].

2.5 Morphology of thin films

The properties of thin films depend largely on their microstructure, which is highly determined by the processes taking place during deposition.

2.5.1 Nucleation and growth

The fundamental processes taking place at the substrate surface are schematically shown in Fig. 2.5. Atoms from the gas phase impinge on a solid surface with a certain arrival rate, and are either adsorbed or directly reflected by transferring their kinetic energy to the lattice. The atoms can diffuse a certain distance before they stick or reevaporate again. Here the diffusion distance and the time of adsorption are determined by the activation energies of desorption and surface diffusion. Therefore, at high impact rates the formation of metastable and stable clusters occurs by binding of diffusing atoms or by a direct impingement of atoms, in other words, condensation occurs. This cluster formation is called nucleation. When the nuclei continuously grow, clusters combine if the nuclei mutually contact, either by growth or by motion. And then a network of connected clusters can be formed by continued coalescence. Finally, a full covered film can be formed [44, 46].

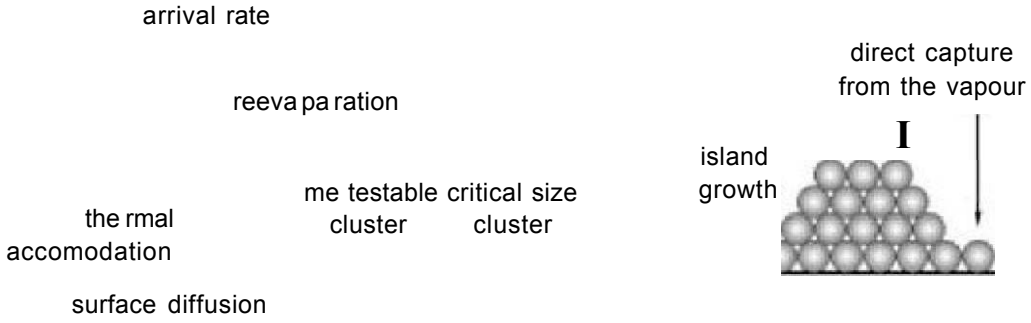

Fig. 2.5: Processes during nucleation and growth of crystals on a substrate **[44],**

Many experimental observations revealed that there are three basic nucleation modes:

(1) Island growth (Volmer-Weber),

(2) Layer growth (Frank-Van der Merwe), and

(3) Island-layer growth (Stranski-Krastonov)

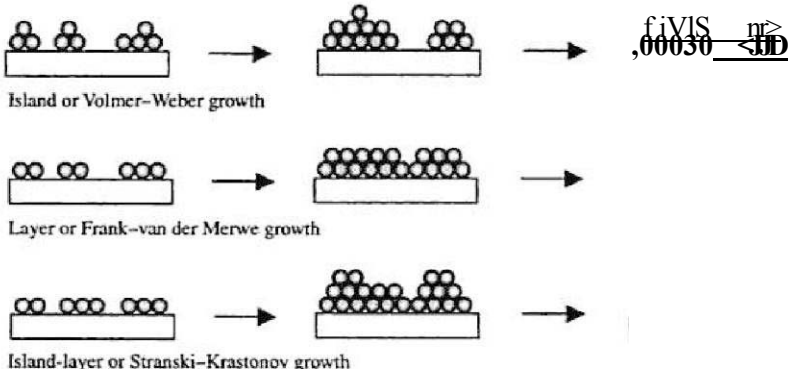

Fig. 2.6: Schematic illustration of the three basic modes of initial nucleation in the film growth [22].

In Fig. 2.6 the different growth modes are schematically illustrated. Especially, the interaction between film and substrate plays a very important role. Usually, if the bonding energy between the growing species is higher than the adsorption energy of the impinging particles on the substrate, a complete island growth (Volmer-Weber mode) takes place. This mode is mostly displayed for many systems of metals on insulating substrate materials during the initial film deposition. In the opposite case, the growing species are more strongly bound to the substrate than to each other, which characterizes the layer growth (Frank-van der Merwe mode), where the nuclei grow in two dimensions on the substrate surface. At first, a complete monolayer is formed, followed by layers with decreasing adsorption energy, which makes the depositions of the atoms easier with increasing layer numbers. For layer growth, the important

examples are the epitaxial growth of single crystal films. In the last case, islands are formed on top of a first continuous layer. This intermediate growth mode is called island-layer growth, combining the both growth modes discussed above [22, 46].

2.5.2 Structure zone model

Thin film structures are mutually determined by the used deposition technique and can be regarded as a strongly nonlinear function of deposition parameters, such as temperature, ion bombardment, pressure, etc. Thus, structure zone models (SZM) were developed that interpret the structural evolution of film growth. In a general way, the atomic journey of nucleation and growth of coatings includes five basic processes: shadowing, desorption, surface diffusion, bulk diffusion and recrystallization. Shadowing is caused by the geometric interaction between the roughness of the growing surface and the angular direction of the atoms that impinge at the surface. The other processes are controlled by the sublimation energy, and the activation energies for surface and bulk diffusion, respectively. These energies are strongly connected with the melting temperature of the coating material. These different basic processes can be expected to dominate in a certain field of the homologous temperature (T/T_m). Here, T is the substrate temperature and T_m is the melting point of the coating material. Therefore, T/T_m is the basis of any SZM. The first SZM was published by Movchan and Demchishin, who prepared their films by electron beam evaporation. They classified the coating structure in three zones depending on T/Tm. A modification of Movchan and Demchishin's SZM was performed by Thornton, who obtained thin films by magnetron sputtering and introduced in a new parameter, the sputtering gas pressure. Thereby, the structure zones are shifted to higher temperatures, when the working gas pressure increases. Thornton's model contains a fourth zone, which is called zone T, between zones 1 and 2 (Fig. 2.7) [44, 47].

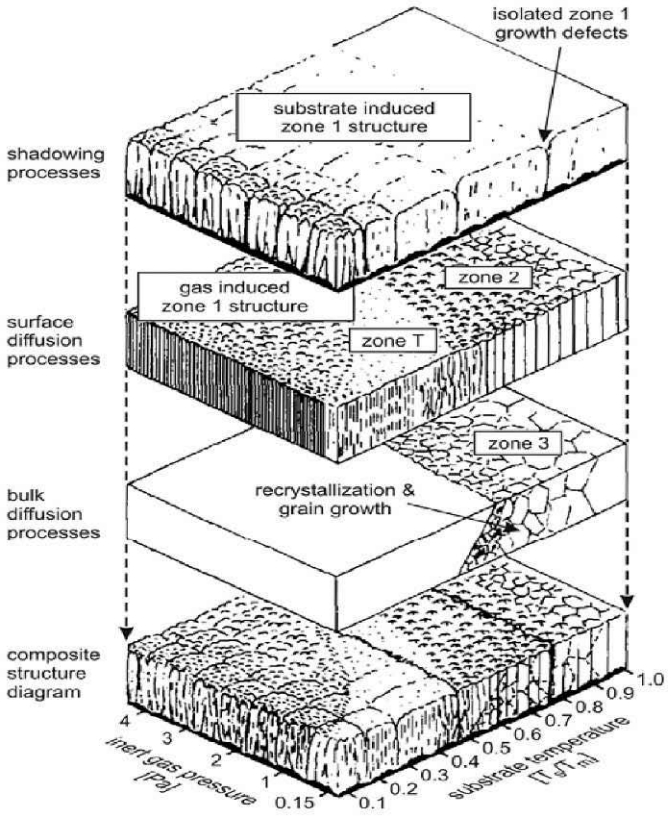

Fig. 2.7: Thornton structure zone model (SZM) consisting of the zones I, T, II and Ill [48].

The various structure zones can be characterized in detail as follows:

-I- ***Zone I*** belongs to a very low temperature interval $0 < T/T_m < 0.2$ where both, surface and the bulk diffusion of atoms is negligible. Therefore, the growth is determined by shadowing effects and low adatom mobility. The microstructure is composed of porous, tapered crystallites separated by voids. The crystals exhibit a high dislocation density and are separated by porous grain boundaries. With increasing T/T_m the diameter of the crystal increases [44, 49].

-I- ***Zone T*** pertains generally to a temperature interval $0.2 < T/T_m < 0.4$ in which the surface diffusion is enhanced, The transition zone between zone I and zone II consists of a dense array of poorly defined fibrous grains without voided boundaries [44, 49].

-I- ***Zone II*** is characterized by high substrate temperatures ($0.3 < T/T_m < 0.5$) at which both surface and grain boundary diffusion occur at significant levels. The grain size further rises with increased T/Tm and the grains may extend through the coating thickness when the process temperature is sufficiently high. Therefore, in this zone columnar grains are formed, separated by distinct and dense intercrystalline boundaries [50].

-I- In ***Zone Ill*** the bulk diffusion plays the dominant role. Therefore, secondary recrystallization of the coating occurs during deposition. This zone consists of equiaxed grains with a high density, resulting in a high surface quality. This structure is generally attributed to the high substrate temperature range ($0.5 < T/T_m < 1$) [49-50].

In practice, the co-deposition of active impurity species is difficult to avoid and are important for the structure formation of polycrystalline films. Therefore, Barna and Adamik investigated the influence of impurity atoms on the development of the structure zones, as illustrated in Fig. 2.8 [51-54].

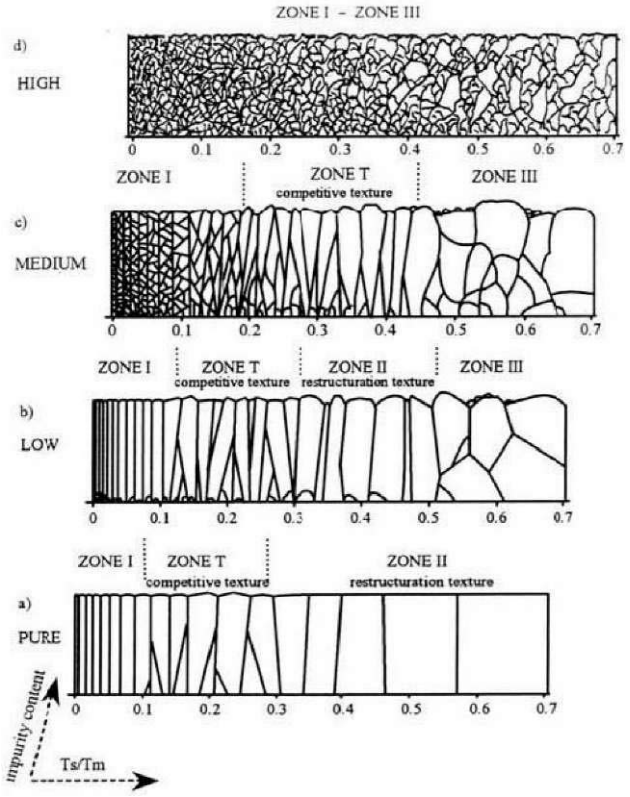

Fig. 2.8: Ideal a) and real SZM at low b), medium c), and high d) impurity content [53].

Impurity species impinging onto the film surface can be adsorbed and segregated on the growing crystal surface or dissolved in the crystal lattice. At first, at low impurity concentration the impurity phase will condense or concentrate only at the grain boundaries. When the impurity concentration is high, the impurity phase will grow over the surface of the neighboring crystals and finally completely cover the surface of the growing crystals, thereby interrupting the growth of the crystals. This causes renucleation. Therefore, new micro- and nanostructures can be created.

As to be seen in Fig. 2.8, the upper boundary of zone I shifts to higher temperatures with increasing impurity concentration. Because of the low adatom mobility, coalescence or grain boundary migration is impossible in this zone and thus grain coarsening is inhibited. In contaminated films, due to be limited grain boundary mobility also the lower boundary of the zone II shifts to higher temperatures. With increasing impurity concentration, the lower boundary of zone III shifts to lower temperatures and finally reaches the upper boundary of zone I. The result is that zone II and zone T vanish one after the other [53].

Due to the huge impact of the ion bombardment energy on the structure of the thin films, the SZM on the basis of Thornton's model was further modified by Messier et al. (Fig. 2.9), including the effects of both thermal, and bombardment-induced mobility. With increasing the bombardment energy, the width of the zone T increases on expense of zone I [54].

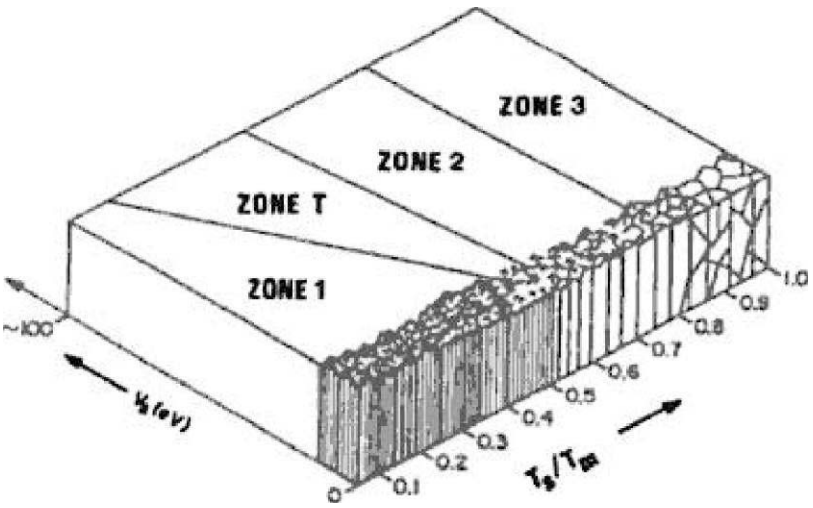

Fig. 2.9: Modified SZM by ion assisted PVD after Messier et al. [54].

3 Coating system

3.1 Binary phase diagrams

Binary phases, such as nitrides and carbides of transition metals, are interstitial compounds [44]. Usually, the nonmetallic atoms (N, C, B), due to their small atomic radius, are embedded into the gaps of a metallic unit cell. Possible interstitial compounds are usually expressed by the following formulas: M_4X, M_2X, MX, MX_2, where M and X separately denote metallic and nonmetallic atoms, respectively. In this thesis, nitrides of transition metals, such as YN und HfN, pertain to the MX type. The crystallographic structure of YN is the face centered cubic B1 structure (prototype NaCl) (Fig. 3.1).

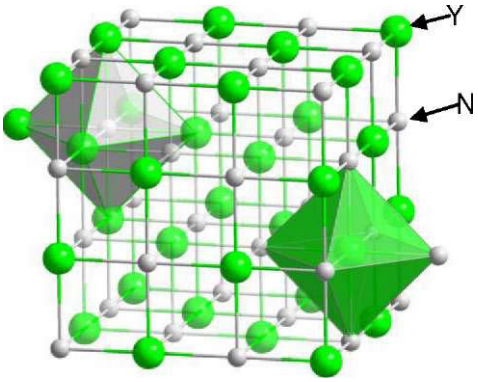

Fig. 3.1: Crystal structure of NaCl with a polyhedral coordination [55].

3.1.1 Y-N

Yttrium is a silvery-metallic, lustrous and trivalent transition metal. The Y-N phase diagram (Fig. 3.2) exhibits three phases, namely: 1) the solid solution (aY), 2) the solid solution (PY), and 3) the nitride YN.

Scandium nitride shares some of AlN's promising physical properties, such as high hardness and mechanical strength, high temperature stability, and excellent electronic transport properties. Thus, ScAlN exhibits semiconducting properties and enables for composition dependent bandgap engineering by varying the amount of Al on the metallic sublattice [56]. Since Y and Sc belong to the same main group (III B) of transition metals, also YAlN is

believed to exhibit comparable semiconducting properties, which can be of significant importance for e.g. piezoelectric applications, where the bigger lattice constant of YN compared to ScN would imply a longer range of the actuator.

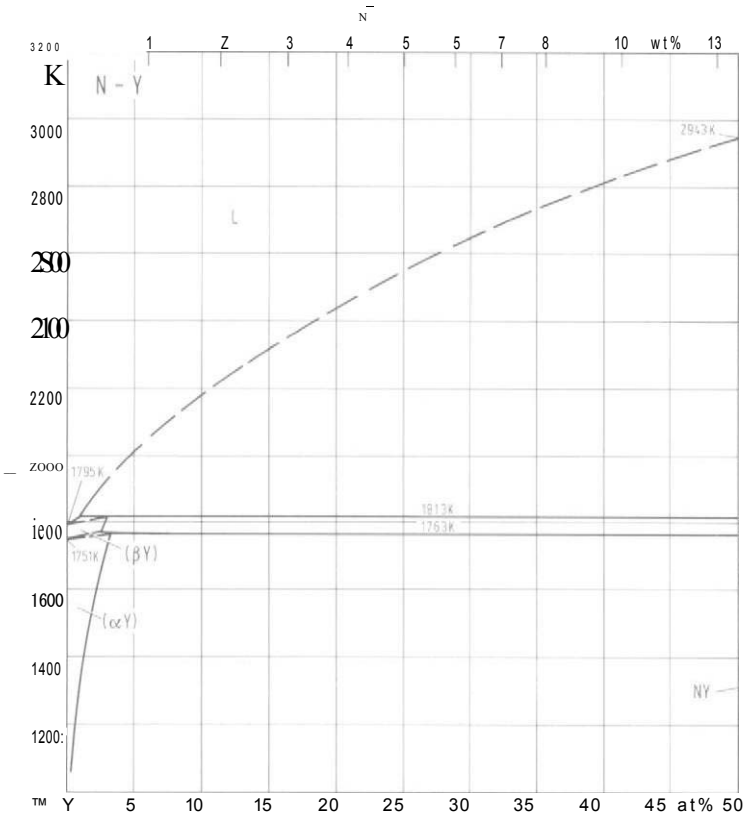

Fig. 3.2: Y-N partial phase diagram (< 50 at% N) [57].

3.1.2 Hf-N

Hafnium is a silvery gray, lustrous and tetravalent transition metal. The equilibrium solid phases of the Hf-N system (Fig. 3.3) are (1) the hcp solid solution (aHf) (2) the solid solution (PHf) (3) the nitride H3N2 (4) the nitride H4N3 and (5) the nitride HfN, which exhibits the highest melting point within the group of transition metal nitrides. The crystal structure and lattice parameters of intermediate phases are summarized in table 3.1.

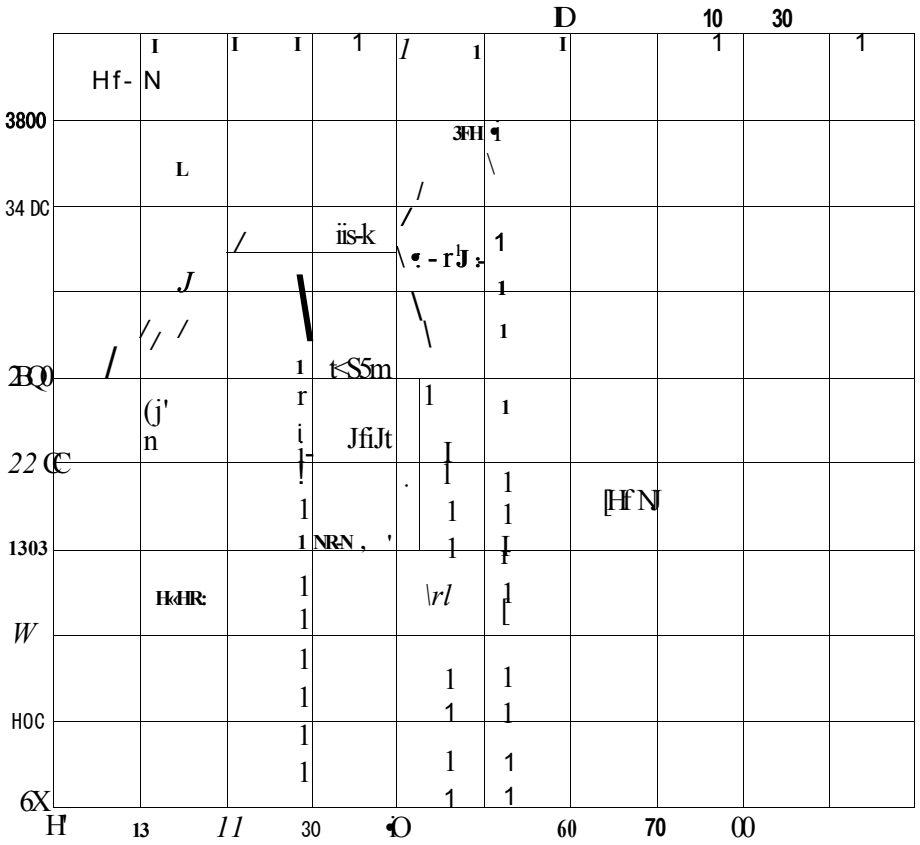

Fig. 3.3: Hf-N phase diagram [58].

Table 3.1: Hf-N crystal structure and lattice parameters of intermediate phases [58].

phase	structure	type	a [nm]	b [nm]
H3N2	hex	AgCrSe2	0.3206	2.326
Hf4N3	hex	C3V4	0.3214	3.112
HfN	cub	NaCl	0.452	-

3.2 The ternary system

The performance of transition metal nitrides such as oxidation resistance and wear behavior is improved by the aluminum incorporation in the transition metal nitride matrix.

Previous studies have shown that a phase change from B1 structure to B4 structure occurs at a

critical AlN content in pseudobinary TM-Al-N (TM: transition metal) films (Fig. 3.3) [59]. Due to this phase transition the film properties change dramatically. For example, the cubic lattice parameter of TLxALN decreases from ~4.24 A for pure TiN to ~4.17 A at x = 0.6 due to increased substitution of Ti atoms by smaller Al atoms. With increasing Al content the mechanical properties increase significantly in the B1 structure due to solid solution hardening, and the mechanical properties begin to deteriorate quickly with the formation of the B4 structure [8, 59-62, 82].

The transition zone of some prominent TM-Al-N (TM: Ti, Cr, Nb) systems are listed in table 3.2.

Table 3.2: Transition zones of several TM-Al-N (TM: Ti, Cr, Nb, Ta) system [63, 82].

TM-Al-N system	Transition zone [at. %-ratio]
TLxALN	0.65 ~ 0.75
Cr,xALN	0.70 ~ 0.77
Nb,xALN	0.44 ~ 0.61
Ta,xAlxN	0.36 ~ 0.65

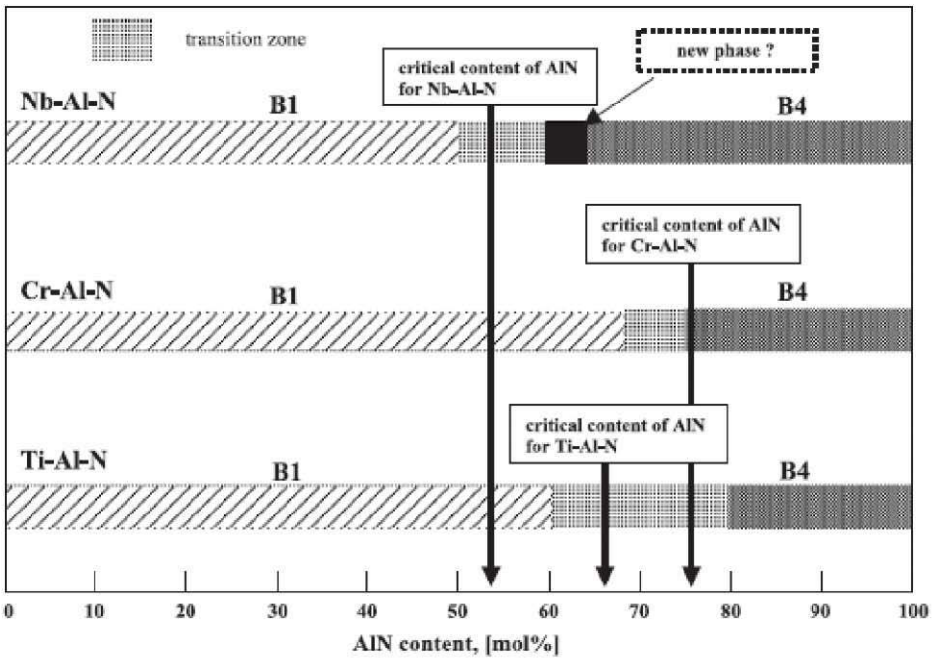

Fig. 3.4: Metastable domains determined experimentally in TM-Al-N (TM: Ti, Cr, Nb) system [59].

4 Experimental

4.1 Coating deposition

4.1.1 Unbalanced magnetron sputtering array

A modified Leybold-Heraeus A-400 lab scale DC reactive magnetron sputtering system with nitrogen as reactive, and argon as working gas is used in this thesis, as schematically shown in Fig. 4.1. Detailed explanation of the sputtering array can be found in [64-68].

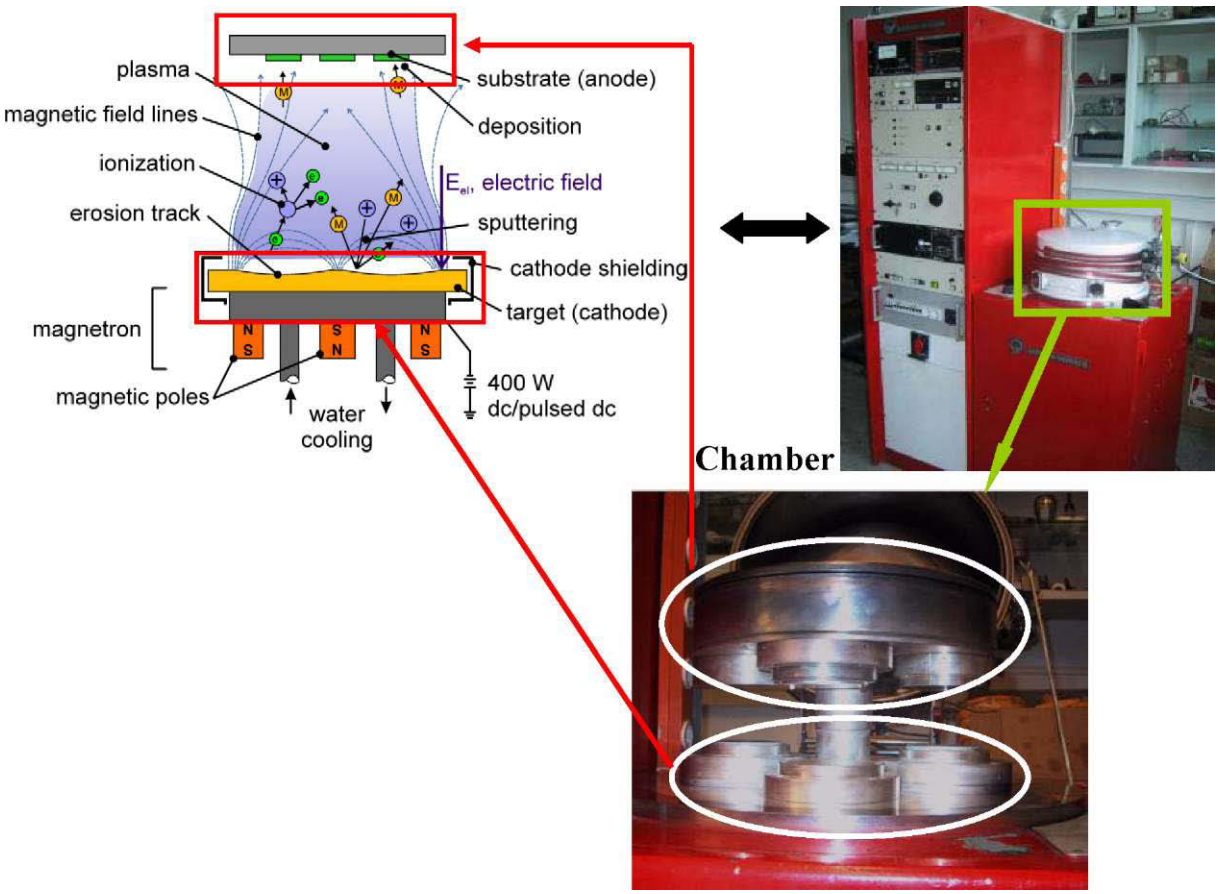

Fig. 4.1: Leybold-Heraeus A-400 unbalanced magnetron sputtering unit [69].

The stainless-steel reaction chamber has a size of 0 420 mm x 200 mm and contains two parts: rotatable upper-part and a fixed lower part (target holder). The rotatable upper-part contains the substrate holder, which can be heated up to 550 ^{o}C, and charged with a bias voltage. The purpose of RF-sputter cleaning of the substrates is achieved by a RF-generator (ENI ACG-6B) before deposition. The lower part at the reaction chamber contains the

magnetrons, the pump flange, the pressure gauges and the gas inlet. All three magnetron cathodes are placed at the bottom of the chamber and are isolated against the chamber walls by a Teflon base plate, where the target-magnetron assembly with 76.2 mm in diameter and variable thickness are mounted. In order to achieve good thermal and electrical conductivity, the targets are bonded with Indium to the cathode. The magnetron includes a circular permanent magnet system (Gencoa PK 75) and a water cooling system at the backside. A Leybold-Heraeus DC sputter generator is used as power supply. During the deposition a DC bias generator (Sorensen DCR 300-1.5) supplies the substrate bias voltage. The evacuation system consists of a pre-vacuum pumping system (rotary vane vacuum pump Pfeiffer DUO 20) and a turbomolecular pump (Leybold Turbovac 361). The working gas Ar flow between 0 to 200 sccm and the reactive gas N_2 flow between 0 to 50 sccm can be independently adjusted and controlled by the gas flow measure- and control-unit (Tylan R0-7031, controller Tylan R0-7030). The chamber pressure is measured by a Leybold Combivac CM 31.

4.1.2 Targets and substrates

All coatings were deposited from either a pure Y-target or powder metallurgically produced Hf-Al compound targets with a Hf/Al ratio of 70/30 or 55/45, see Table 4.1. As substrates silicon wafers with (100) orientation and a size of 7 x 20 x 0.5 mm were used in this thesis. Coating characterization, including X-ray diffraction analysis, scanning electron microscopy, nanoindentation and thickness evaluation, was performed for all coatings on Si.

Table 4.1: Target materials used.

Target composition	Dimension [mm]	Purity [%]	Manufacturer
Yttrium	0 76.2 X 5	99.9	MaTeck
Hf0.70Al0.30	0 76.2 X 5	99.9	Plansee AG
Hf0.55Al0.45	0 76.2 X 5	99.9	Plansee AG
Al-Plates	0 5X2	99.9	MaTeck

For the deposition of the ternary coatings additional pure Al-platelets were placed on the race track of the Y- or Hf-Al-targets, respectively. The Al content in the ternary coatings was increased by increasing the number of Al-platelets on the target, see Fig. 4.2.

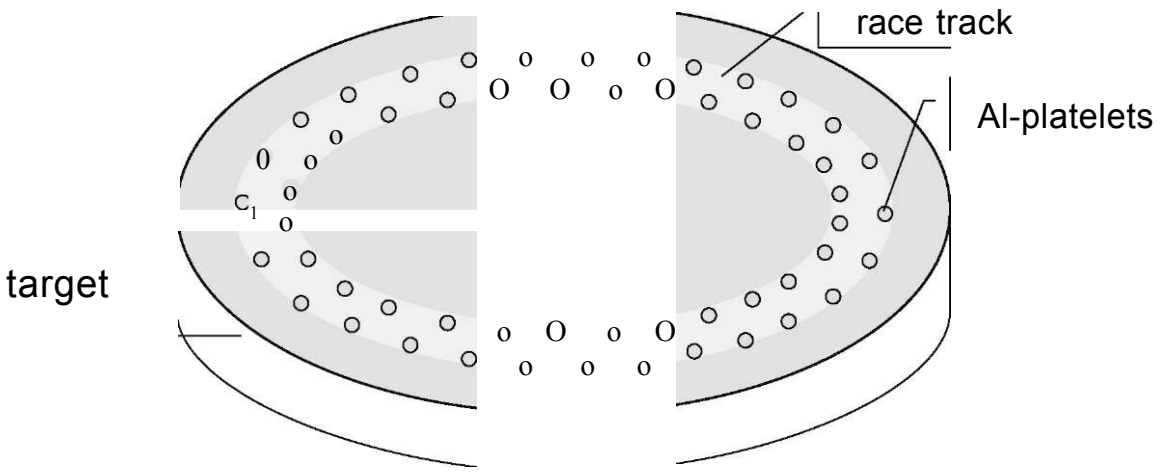

Fig. 4.2: Schematic drawing of the Al-platelet position on the Y- or Hf-Al targets.

4.1.3 Deposition procedure

The deposition procedure is usually composed of the following steps:

1. Since the surface conditions of the substrate directly influence the quality and performance of the deposited coating, sufficient cleaning of the substrate is an important step before the deposition. In this thesis, this cleaning process of the substrate was carried out in successive supersonic baths: At first, in order to remove the organic matter of the substrate surface, the substrates are cleaned in acetone for 5 min, and then cleaned again in alcohol for another 5 min.
2. Then the cleaned substrates are quickly dried, placed on the substrate holder and mounted in the vacuum chamber.
3. After pre-evacuation to 10^{-1} Pa, to support degassing and desorption process, the chamber wall is heated up to ~100 ^{o}C by external heating and the substrate holder is heated up to 500 ^{o}C through the substrate heating for 60 min.
4. After cooling for about 45 min, a base pressure of $< 3 \times 10^{-3}$ Pa is reached. Subsequently, the internal heating is activated for 15 min.
5. Then the sputter cleaning of the target is performed for 5 min in Ar-atmosphere at 400 W. The substrate holder is rotated away from the location where the substrates would face

the target in order to avoid substrate contamination.

6. Subsequent RF-plasma etching of the substrates with 100 W was carried out for about 10 min in order to clean the surface of the substrate prior to deposition. During this procedure the DC-power was reduced to 80 W, only to sustain the plasma. The pressure is ~ $1.2x10^{-2}$ Pa.
7. After substrate cleaning the power is increased again on the DC sputter generator to 400 W, and the process parameters, such as Ar-gas- and N-gas flow, were set to the required value at the same time. The substrate is back-rotated to face the target and the RF-generator is switched off.
8. During the deposition process, all deposition parameters were kept constant until the desired coating thickness is reached. The different deposition times used stem from the different target materials, respectively, in order to achieve ~ 3p,m thick coatings.
9. After deposition, the samples were cooled down to room temperature under vacuum conditions, before the pumping system was stopped.

4.2 Coating characterization

4.2.1 X-ray diffraction (XRD)

X-ray diffraction is one of the most frequently applied techniques in the field of structure characterization. XRD is a non-destructive method to derive information on the fine structure of materials - crystal structure, crystallite size, lattice strain, state of ordering.

The resulting diffraction pattern of a substance is, therefore, like a fingerprint of the substance, due to the interference of scattered X-rays where constructive interference occurs only if Bragg's law is fulfilled [70]:

$$n*X = 2*dhkl*\sin 9 \qquad (4.1)$$

Here, n is the order of the reflection, X is the wavelength, d_{hkl} is the distance between two lattice planes and 0 is the diffraction angle.

In this thesis a Siemens D500 diffractometer (Fig. 4.3) in a Bragg / Brentano configuration with CuK_a radiation was used to determine the structure and phase composition of coatings.

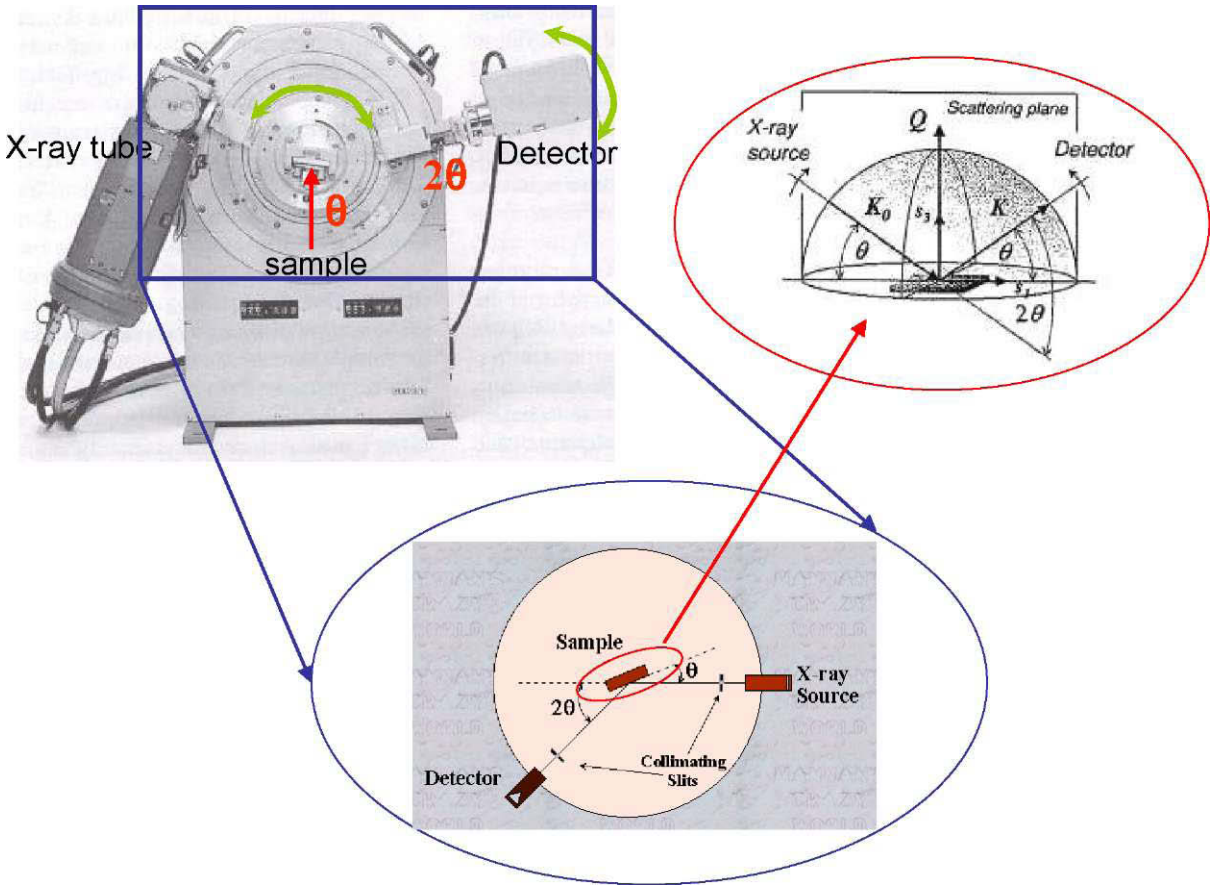

Fig. 4.3: X-ray diffractometer and 0-2θ scan mode by XRD.

The relevant parameters used for the diffraction experiments are summarized in table 4.2.

Table 4.2: XRD-parameters used for the investigations.

XRD-type	CuK-Radiation [A]	High voltage [kV]	Tube current [A]	Time step [s]	Step size [° min^{-1}]
Siemens D500	1.54056	40	25	1.2	0.02

The sample, irradiated by a monochromatic X-ray beam at an angle 0, generates a diffracted beam at an angle 20 from the incident beam, if the lattice planes with orientation planar to the surface of the specimen (certain lattice spacings d_{hkl}) fulfill the diffraction condition according to Bragg's law. By scanning over a selected angular range, a 0 - 20 scan is obtained, as shown in Figure 4.3. Every reflex detected at a certain value of 20 is characteristic for an interplanar lattice spacing d_{hkl}. Thus, by comparing peak position (20) and the corresponding peak height

(intensity) with data from JCPDS (Joint Committee on Powder Diffraction Standards) the peaks can be identified [71-72].

4.2.2 Coating thickness evaluation

The coating thickness strongly impacts the measurement of the mechanical properties of the coatings, such as hardness or residual stress. Especially during nanoindentation the indentation depth should be retained within the topmost 10% of the coating thickness, see section 4.2.3. Therefore, a knowledge of the coating thickness is very important. In order to establish unified testing conditions the coating thickness was controlled to be in the range of about 3p,m in this thesis. The coating thickness was determined by the ball crater technique (Calo®-test). The coated sample was grinded through by a rotating steel ball with a diameter (D) of 25.4 mm using liquid diamond suspension (1p,m) to achieve a circular abrasive wear track, as schematically shown in Fig. 4.4. The inner (D_i) and outer (D_0) diameters of the resulting spherical calotte were then measured by an optical microscope attached with a CCD camera.

Finally, according to the measured value, the coating thickness (t_c) was calculated by the following equation: [73]

$$t_c = \frac{\left(D_0^2 - D_i^2\right)}{4D} \tag{4.2}$$

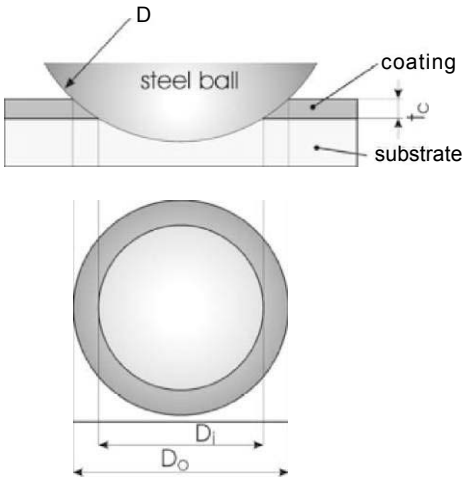

Fig. 4.4: Schematic of the ball crater technique (Calo®-test) [73].

4.2.3 Nanoindentation

In order to determine the mechanical properties of thin films, such as hardness, Young's modulus, strain-hardening exponent, yield strength, fracture toughness or residual stress, nanoindentation was developed in the 1980s [75]. Conventional hardness measurements usually evaluate the residual impression area after the indentation procedure. Thin films however require smallest indents in order not to exceed ~10% of the film thickness [74], to effectively avoid substrate influences. An optical measurement of the plastically deformed zone is thus impossible, which can be overcome by the nanoindentation technique. Nanoindentation primarily consists of a steadily increasing load applied through an indenter that is placed into contact with the flat surface of the specimen. The penetration depth (h) is recorded as a function of the applied load resulting in a load (P) versus displacement curve (Fig. 4.5).

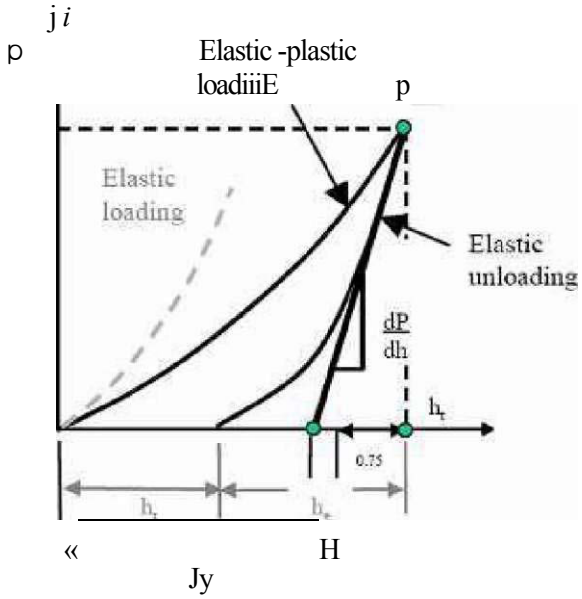

h_r.... residual indentation depth h_e.. ..elastic indentation depth

h_p.. ..contact indentation depth h_t.. ..total indentation depth

Fig. 4.5: Load-displacement curve in a typical hardness experiment [76].

The load-displacement curve indicates that the material undergoes both elastic and plastic deformation. If the load applied to an indenter is released, thus the material attempts to return to its original shape. The modulus and hardness of thin films can be determined by the slope of the elastic unloading region (dP/dh) [74].

In this thesis, a UMIS nanoindenter using a three-sided Berkovich indenter with a face angle of 65.27° was employed [76]. A minimum load of 8 mN, was used and gradually increased with each new indent on a sample to ~18 mN, which is called plateau test. In order to obtain a good statistic of the measured data at minimum 20 indents per coating were performed [77].

4.2.4 Scanning electron microscopy (SEM)

A Zeiss Evo50 Scanning Electron Microscopy was used to investigate the fracture cross-sections and the chemical composition of the coatings. Images of the fracture cross-sections were acquired by secondary electron emission from the sample surface following the excitation by the primary electron beam (acceleration voltage 30 KV). During cross-sectional SEM investigations, the coating thickness and the thickness of the oxide layer were also measured.

The chemical composition of the coatings was determined with an attached Link Systems energy-dispersive X-ray analysis (EDX) calibrated with standards. The coating, which is irradiated by high energy primary electrons, emits characteristic X-rays from shells near the core of the coating atoms. The energy of the emitted X-rays is characteristic for each element. Therefore, it is possible to determine which elements are present in this coating and where these elements are located [78].

5 Results and discussion

All thin films investigated in this thesis were produced on silicon substrates by unbalanced magnetron sputtering using N2 as reactive gas and Ar as working gas at different or constant partial pressures (P_{N_2}/PT).

The following constant parameters were used for all coatings in this thesis:

4- Substrate temperature: 500 °C
-I- Bias voltage : -50 V
4- DC-power : 400 W
4- Total pressure : 0.257 Pa ($2.57*10^{-3}$ mbar)

5.1 Binary system

5.1.1 YN_z-coatings

5.1.1.1 Deposition parameters

In order to obtain various YN_z compositions, the required N_2 partial pressure was adjusted for each deposition. As shown in Table 5.1 the N_2 partial pressure was achieved by variation of the N_2/Ar gas ratio. The N_2 gas flow was increased from 0 to 12.5 sccm while at the same time the Ar gas flow was decreased from 14 to 4 sccm to obtain an increasing N_2-partial pressure ratio, while remaining a constant total pressure of ~ $2.57*10^{-3}$ mbar.

Table 5.1: Overview of deposition parameters.

Ar [sccm]	N2 [sccm]	I [A]	U [V]	PN2/PT [%]
14	0	1.19	319	0
12	1.6	0.99	381	10
11	3.4	1.03	364	20
10	5.1	1.24	306	30
9	7.9	1.40	269	40
7	8.9	1.51	251	50
6	9.2	1.55	245	60
4	12.5	1.58	240	70

5.1.1.2 Phase composition (XRD)

As shown in Fig. 5.1, with increasing the N_2 partial pressure (P_{N2}/P_T) from 0 % to 10 %, no fcc-YN phase, but a high amount of the base-centered monoclinic-Y_2O3 and the body-centered cubic-Y_2O_3 phase, can be identified by comparison to JCPDS data sheets. The peaks detected at a 2θ angle of ~ 54.48 ° (222), 72.44 ° (420) and 86.72 ° (511) by XRD, further exhibit the presence of metallic Y at low P_{N2}/P_T (0-10 %).

Increasing P_{N2}/P_T up to 20 % - 30 % results in the formation of a new phase which is clearly stated by two distinct peaks at 2θ ~ 31.75 ^{0} and ~ 36.83 ° corresponding to fcc-YN. This fcc-YN phase forms at the expense of metallic fcc-Y. This coating is referred to as a mixed structure of fcc-YN, base-centered monoclinic-Y_2O3 and body-centered cubic-Y_2O_3 phase, where the fcc-YN phase clearly dominates.

In the range of P_{N2}/P_T = 40-70 % a single phase structure of a stoichiometric fcc-YN can be found. Both base-centered monoclinic-Y2O3 and the body-centered cubic-Y2O3 phase completely disappeared. By further increase of P_{N2}/P_T the (200) peak at a 2θ angle of ~ 36.7 ° broadens. As PN2/PT is increased to 60 % the peak appearing at a 2θ angle of ~ 36.83 ° (200) achieves it's maximum width. The peak broadening may be a result of grain refinement but can also indicate an increase of residual stress in the films.

Further the (111) orientation gradually increases with increasing P_{N2}/P_T above 30% at the expense of the (200) orientation (compare PN2/PT = 20% and 30%). The coatings are highly

textured with a preferred (111) orientation (20 = 31.75^ , if the P_{N2}/P_T is higher than 30%. Hence, it is legal to say that P_{N2}/P_T has an important impact on the crystal orientation of the coatings deposited. Simultaneously, the peaks shift towards smaller angles with increasing PN2/PT up to 70%.

The results obtained indicate that a stoichiometric YN of high crystal quality is formed for P_{N2}/P_T of 20%. Higher P_{N2}/P_T obviously lead to a preferred (111) orientation and superstoichiometric YN_z films with larger lattice constants, as to be seen in Fig. 5.2.

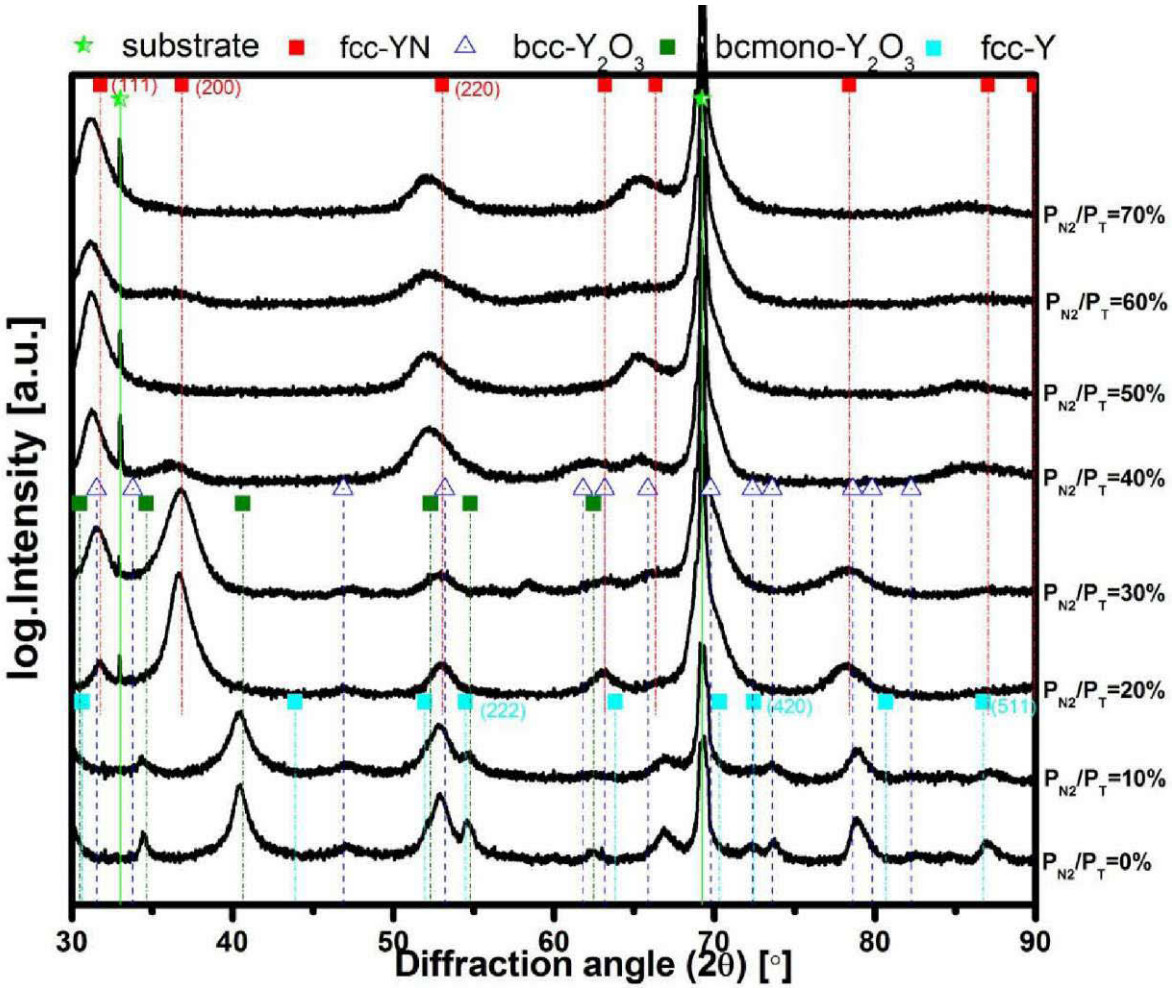

Fig. 5.1: XRD-pattern of the YN_Z coatings as a function of P_{N2}/P_T during deposition, measured approximately 1 hour after deposition.

5.1.1.3 Lattice parameter of YN_z-coatings

The change of the lattice parameter of the YN_z-coatings resulting from an increase of P_{N2}/P_T is summarized in Fig. 5.2, using the position of the (111) peak for determination of the lattice

parameter. In the range from 20 % to 40 % of P_{N2}/P_T the lattice parameter displays a sharp upward trend from 4.875 A to 4.948 A. A further increase of P_{N2}/P_T from 40 % to 70 % leads to a slight increase of the lattice parameter from 4.948 A to 4.968 A. It is assumed that an increase of the lattice parameter is caused because of a supersaturation of the fcc-YN crystal at high N_2/Ar ratios.

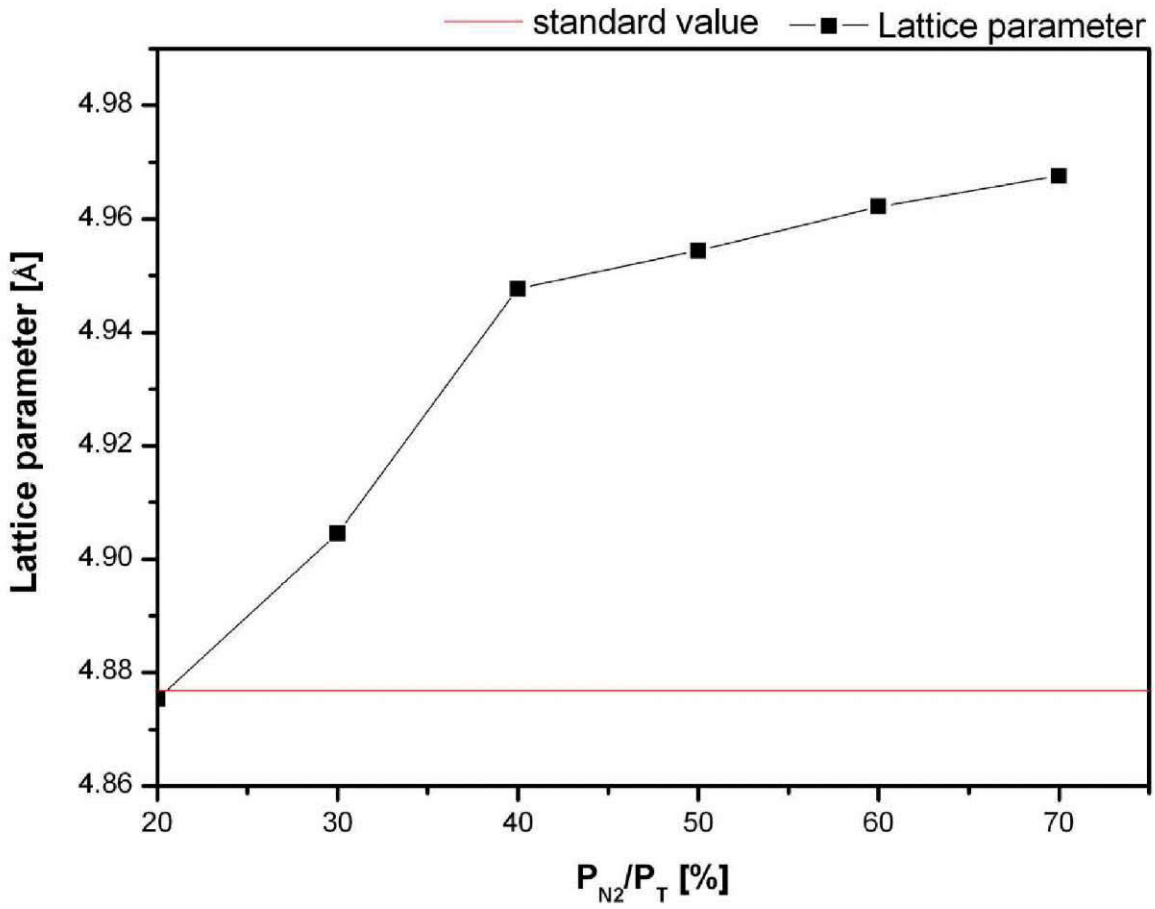

Fig. 5.2: Lattice parameter of YN_z-coatings with increasing P_{N2}/P_T during deposition.

5.1.1.4 Oxidation

Figure 5.3 displays the change of the coatings with increasing P_{N2}/P_T during deposition after one week in ambient air. The film with lowest N_2 partial pressure (P_{N2}/P_T = 10 %), corresponding to a mixed structure of bcc-Y and base-centered monoclinic-Y_2O_3 and body-centered cubic-Y_2O_3, exhibits a relatively smooth surface with gray color. An increase of P_{N2}/P_T from 20 % to 30 % results in the formation of partial oxide layer (white color) on the

surface, see Fig. 5.3 c), d). In the range of 40-70 % P_{N2}/P_T the color of the surface begins to change immediately after exposure to air. A white oxide layer is formed on the surface within already one day. With increasing exposure time in ambient air, the oxide layer increases until even the oxide layer spalls off from the surface, see Fig. 5.3 e), f), g), h). This indicates that the oxidation rate strongly depends on the initial structure after deposition and therefore on the N_2 partial pressure (P_{N2}/P_T) during deposition.

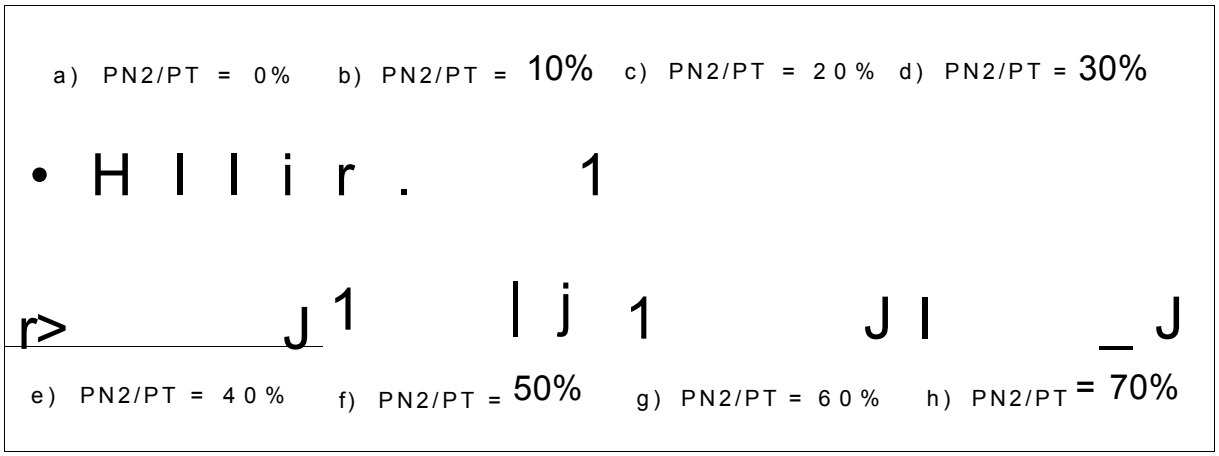

Fig. 5.3: The surface of the sample as a function of the P_{N2}/P_T after one week in ambient air.

Figure 5.4 shows optical microscopy investigations of the surface morphology of the YN_z coatings with an increasing P_{N2}/P_T from a) 10 % to b) 20 % to c) 30 % to d) 40 % to e) 50 % to f) 60 %, respectively, after exposure in ambient air for three months. The surface of the YN_z coating a) exhibits a very porous structure. With an increasing P_{N2}/P_T from b) to f) the surface exhibits a relatively dense structure compared to the surface of a). An increasing P_{N2}/P_T from 20% b) to 30% c) leads to a monochrome surface. A further increase of P_{N2}/P_T from 30% d) to 50% f) leads to the formation of a polychrome surface, see Fig. 5.3. Additionally it is possible to identify cracks on the surface in the samples with 30%, 40%, 50% and 60% P_{N2}/P_T, see Fig. 5.4, which might be caused by cracked pores.

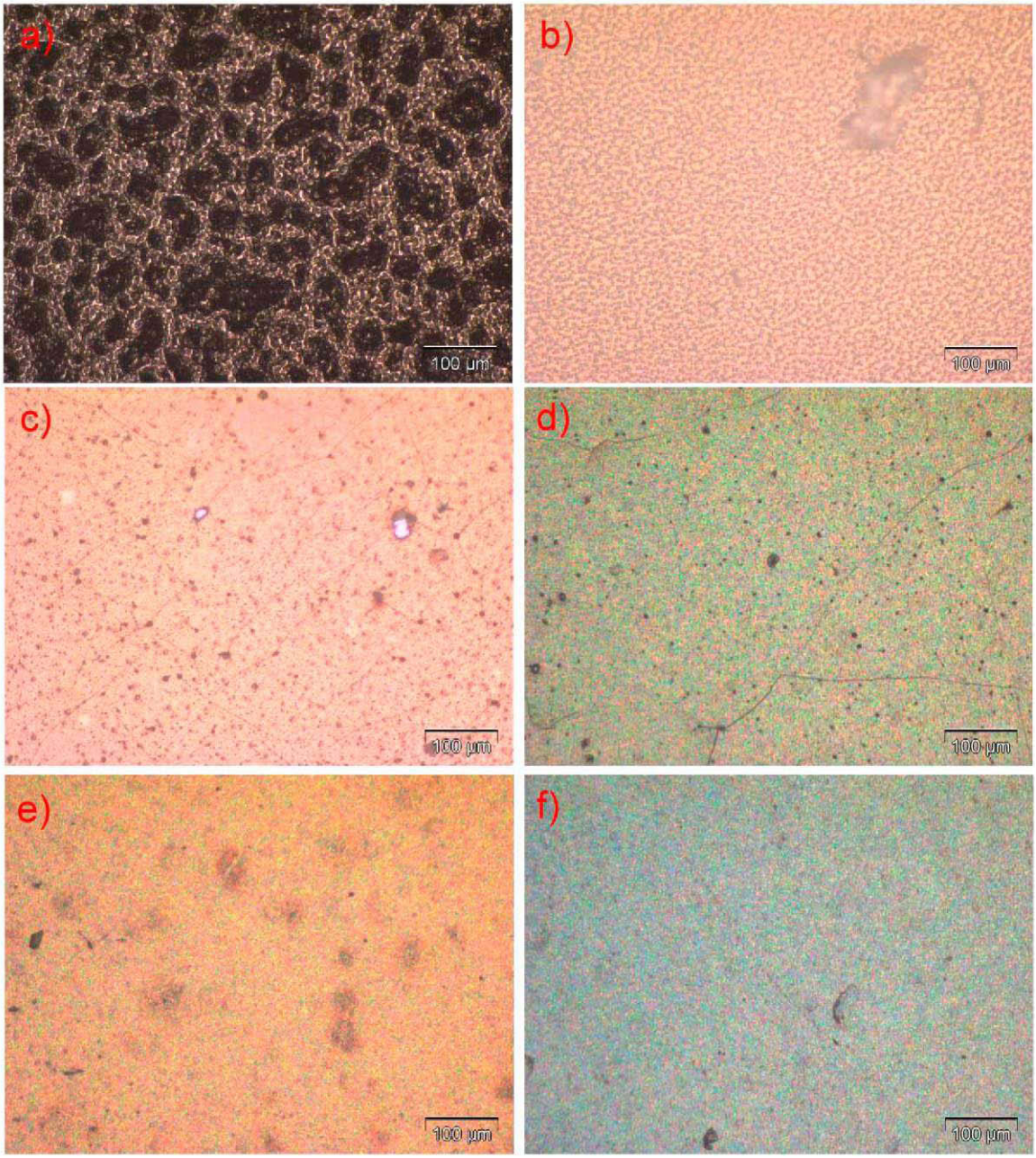

Fig. 5.4: The oxidation behavior of YN_z coatings with increasing P_{N2}/P_T after 3 months (optical micrographs) a) 10 % b) 20 % c) 30 % d) 40 % e) 50 % f) 60 %.

5.2 Ternary system

In this thesis, both ternary systems ($Yi_{-x}Al_xN$ and $Hf_{1-x}Al_xN$) are obtained by using powder-metallurgically produced targets in a mixed argon-nitrogen atmosphere, where the gas flow of argon and nitrogen were fixed to 9 and 7.9 sccm (P_{N2}/P_T = ~40%), respectively.

5.2.1 Y1-xAlxN-coatings

From the previous section, it is clear that the yttrium nitride crystals readily oxidize in air at room temperature. In order to improve the oxidation resistance of YN_z-coatings, addition of pure Al-platelets were used on the yttrium target race track to control the Al-content in the $Y_{1-x}Al_xN$ ternary coatings, see chapter 4.1.2. With increasing number of the Al-platelets the Al content increases according to Table 5.2.

Table 5.2 shows the compositions of the $Y_{1-x}Al_xN$-Coatings measured by EDX analysis. The information depth depends on the density of the tested substances and emitted characteristic X-ray such as K_a, Kp. For iron with a density of 5.6 g/cm the information depth is ~800 nm for an acceleration voltage of 15 kV. The density of Silicon is 2.33 g/cm^3 and the information depth is thus estimated to be ~3000 nm. Hence the information depth strongly depends on the density of the investigated material. The thickness of the growing oxide layer containing yttrium oxide (p = 5.01 g/cm^3) and alumina (p = 4 g/cm^3) of the coatings increase up to 300 nm after one week in ambient air. Taking into account the smaller density of the oxides, it can be assumed that the information depth of the chemical composition of the coatings is more than 300 nm. In other words, the measured chemical composition (Table 5.2 and 5.3) include the oxide layer and coating.

The determination of the chemical compositions one day after deposition shows that the oxygen content in the coatings decreases with increasing amount of aluminum. The sum of non metallic species (oxygen and nitrogen) maintain roughly a constant value of ~52.52 at.%. Thus, the incorporation of oxygen is meant to take place on nitrogen sites of the non-metallic sublattice. For the further discussion a nomenclature of the coatings was chosen which refers to a normalization of the metallic species and assuming a N-content of 50%.

Table 5.2: Compositions and coating nomenclature of $Y_{1-x}Al_xN$-coatings measured after 24 hour.

Number of Al-platelets	coating nomenclature	O/(N+O) at.%-ratio	elemental composition (at.%)					Al/(Al+Y) at.%-ratio
			Y	Al	O	N	N+O	
8	Y0.71Al0.29N	0.52	30.21	12.22	29.69	27.88	57.57	0.29
12	Y0.56Al0.44N	0.21	25.92	20.36	11.10	42.62	53.72	0.44
16	Y0.4sAl0.52N	0.16	23.38	25.03	8.05	43.54	51.59	0.52
20	Y0.47Al0.53N	0.10	22.73	25.50	4.93	46.85	51.78	0.53
24	Y0.44Al0.56N	0.10	21.92	27.69	4.91	45.48	50.39	0.56
28	Y0.41Al0.59N	0.06	20.51	29.41	3.10	46.98	50.08	0.59

The oxygen content of the $Y_{1-x}Al_xN$-coatings after one day and after one week is listed in Table 5.3 and graphically summarized in Figs. 5.5 and 5.6. Comparing the O/(N+O) at.%-ratio, the oxygen content of the $Y_{1-x}Al_xN$-coatings with different Al content show a clear trend with increasing exposure time in ambient air. An increase of the Al content, results in significantly lower O/(N+O) at.%-ratio.

Table 5.3: A comparison of the oxygen content of the $Y_{1-x}Al_xN$-coatings after one day and after one week.

Al/(Al+Y) at.%-ratio	after one day (at.%)				after one week (at.%)			
	O	N	N+O	O/(N+O)	O	N	N+O	O/(N+O)
0.29	29.69	27.88	57.57	0.52	55.37	12.85	68.22	0.81
0.44	11.10	42.62	53.72	0.21	25.64	31.38	57.02	0.45
0.52	8.05	43.54	51.59	0.16	18.03	38.25	56.28	0.32
0.53	4.93	46.85	51.78	0.10	10.32	40.7	51.02	0.20
0.56	4.91	45.48	50.39	0.10	8.1	41	49.1	0.16
0.59	3.10	46.98	50.08	0.06	4.91	45.53	50.4	0.10

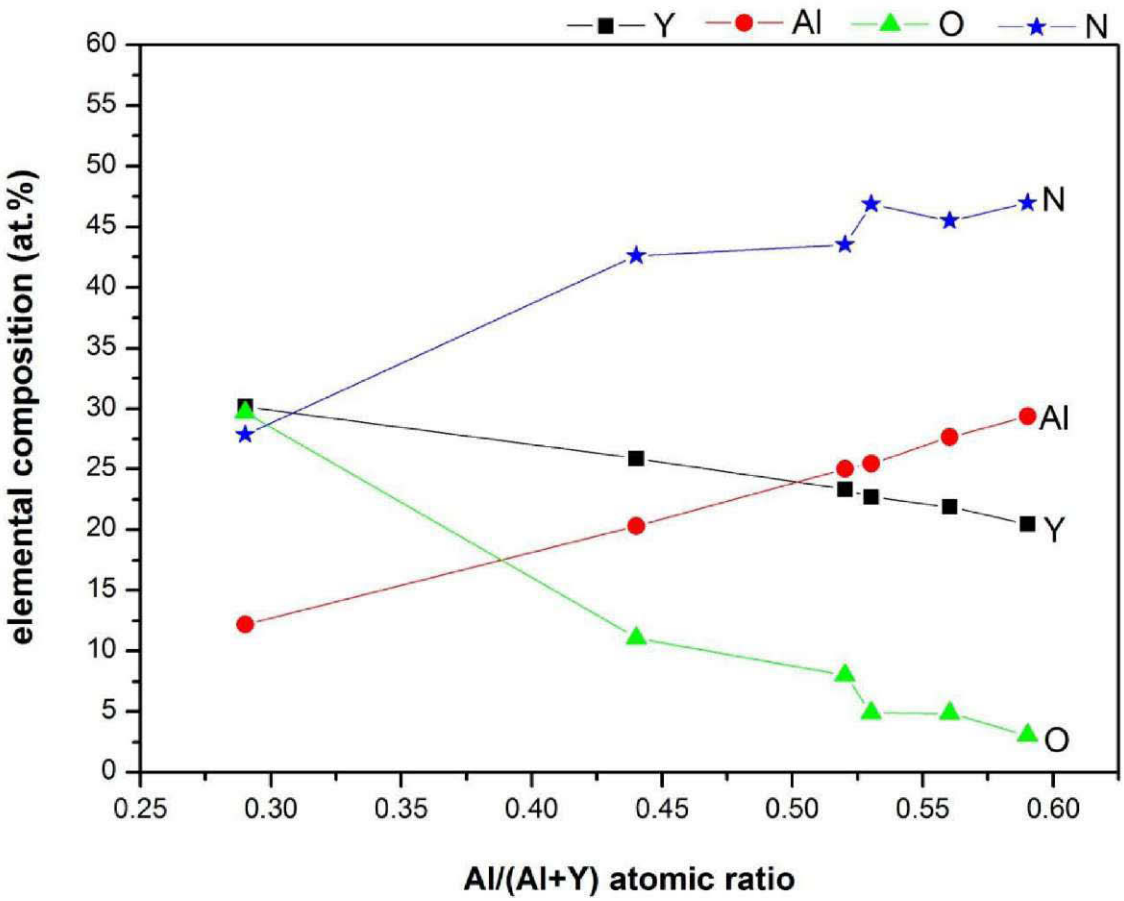

Fig. 5.5: Elemental composition of Y, Al, O and N as a function of Al/(Al+Y) atomic ratio after one day.

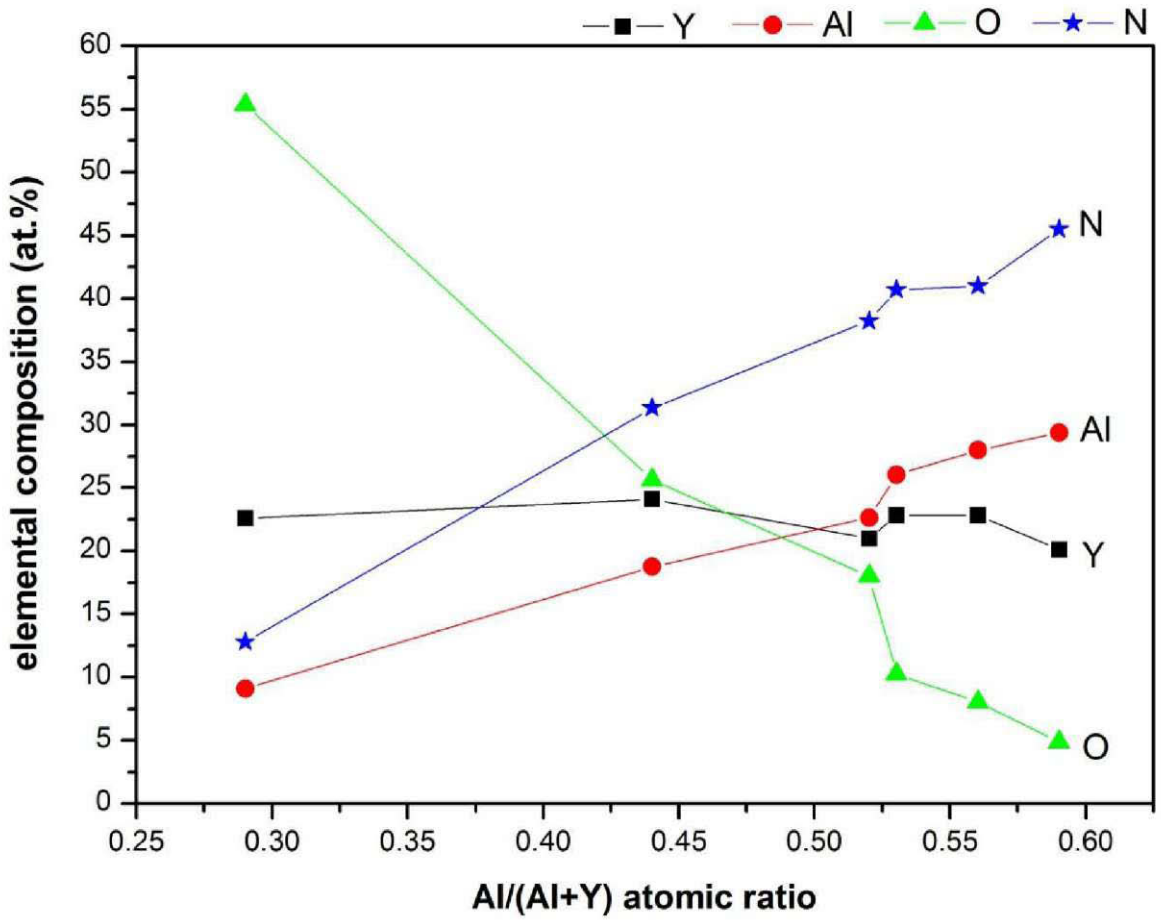

Fig. 5.6: Elemental composition of Y, Al, O and N as a function of Al/(Al+Y) atomic ratio after one week.

5.2.1.1 Phase composition and structure analysis (XRD)

Figure 5.7 shows the XRD-pattern of the $Y_{1-x}Al_xN$ coatings with increasing Al content. The pattern at the bottom results from a YN_z coating, deposited at P_{N2}/P_T = 40%, which was kept constant for all other Al-containing coatings. With increasing amount of Al in the coatings, the incorporation of Al occurs presumably at Y lattice sites, as only a single phase cubic solid solution can be identified. In the range from 21 at.% to 29 at.% Al content also results in a shift of the peak at 20 ~ 35.55 ° to higher angles, i.e. the peak shifts towards the cubic AlN peak position. This is caused by substitution of Y by Al atoms, and therefore, the parent fcc-lattice decreases due to small atomic radius of aluminum atoms. Also the cubic (200) orientation strongly increases in intensity for Al-amounts up to ~29 at.%. At the same time, the (200) peak at 20 ~ 36.71° broadens, which may be caused by grain refinement. This

development is consistent with the conclusions drawn from SEM investigations (see Fig. 5.8a). A further increase in the Al content up to 37 at.% at the metallic sublattice causes no further shift to higher diffraction angles and a loss in intensity. This indicates an Al-saturation of the c-$Y_{1-x}Al_xN$ solid solution phase and the formation of a second metastable phase, although the cubic reflex dominates in the XRD pattern. An amount of 44 at.% Al in the coating causes a further decrease in X-ray intensity and an intense peak broadening, which can be attributed to extensive grain refinement resulting from the formation of a two phase structure of c-$Y_{1-x}Al_xN$ and w-$Y_{1-x}Al_xN$. The corresponding w-$Y_{1-x}Al_xN$ (002) peak can be found at 2θ ~ 35.55 ° With further increasing the Al content from 52 at.% to 62 at.% a single phase structure of w-$Y_{1-x}Al_xN$ forms at the expense of c-$Y_{1-x}Al_xN$. The peak at 2θ ~ 32.87 ° (100) shifts to higher angles, which is caused by the grain refinement and consistent with the obtained results from SEM (Fig. 5.8 d), e), f)). Hence, a transition from a single phase cubic structure towards a mixed dual phase structure composed of c-$Y_{1-x}Al_xN$ and w-$Y_{1-x}Al_xN$ occurs for an Al content of ~ 37 at.%, before a wurtzite phase dominated regime of $Y_{1-x}Al_xN$ is obtained for Al contents > 44 at.%.

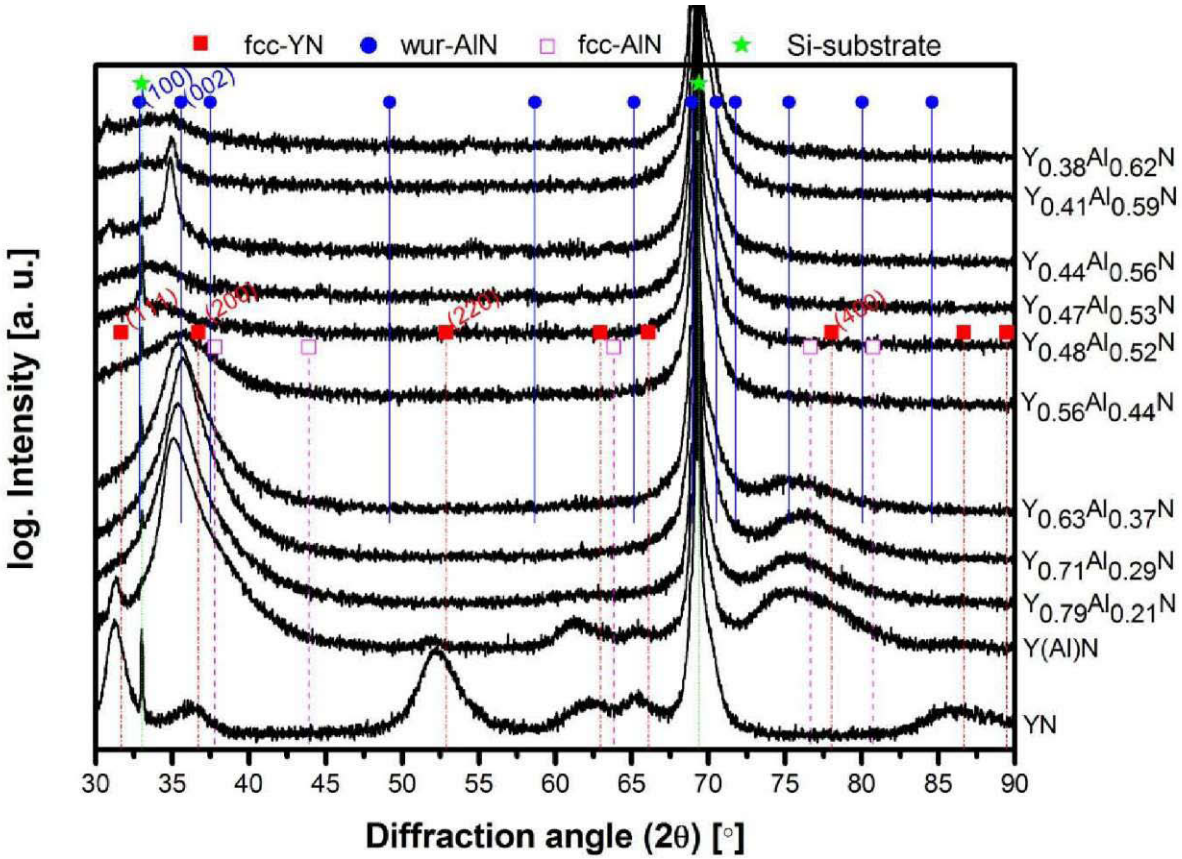

Fig. 5.7: XRD-patterns of the $Y_{1-x}Al_xN$ coatings with increasing Al content after deposition.

5.2.1.2 Oxidation

The coating morphology of the $Y_{1-x}Al_xN$ coatings, exposed to ambient air for 5 weeks, is displayed by SEM cross-sections of some representative coatings, see Fig. 5.8. In Fig. 5.8a it is clearly visible that the unoxidized part of the single phase c-$Y_{1-x}Al_xN$ coating with 29 at.% Al exhibits a dense columnar structure. With increasing the Al content up to 44 at.% (Figs. 5.8 b, c) the column width increases, but also the growth direction is slightly tilted with respect to the substrate normal, stemming from the formation of w-$Y_{1-x}Al_xN$ phase in the films. This behavior agrees well with literature reports on Ti-Al-Y-N films, where a perpendicular growth direction dominates in the single phase cubic regime, and the coatings composed of a mixed cubic and hexagonal structure exhibit an increasing tilt of the growth direction with increasing amount of hexagonal phase [79].

As soon as the single phase w-$Y_{1-x}Al_xN$ phase field is entered for Al-additions of ~52 at.%, the column width abruptly decreases before, with further increase of the Al-content a sequential increase of the column diameter can be observed again.

The structural development of the $Y_{1-x}Al_xN$ films can be interpreted by taking into account the impurity (oxygen) concentration of the respective coatings, compare Table 5.2, According to the structure zone model of Barna and Adamik, see chapter 2.5.2, the incorporation of impurity atoms act as renucleation centers during film growth. As a high oxygen concentration can be detected for the films with Al contents up to ~52 at.% the observed phenomena can be explained by the formation of an $Y_{1-x}Al_x(O,N)$ solid solution. The increasing Al content in the coating effectively reduces the incorporation of oxygen, which can be regarded as an impurity species for Al contents above 53 at.%. Hence, a further increase of the Al content from 53 at.% to 59 at.% results in a very fine grained structure, in agreement with Barna' SZM, respectively, which causes an almost featureless appearance in the cross-sections of the high Al-containing $Y_{1-x}Al_xN$ coatings (see Fig. 5.8).

Further, the oxide scale formation after 5 weeks in ambient air can be observed in Fig. 5.8 from the SEM cross-sections. The oxide layer of the coating containing 29 at.% Al exhibits a thickness of about 0.553 p,m (Fig. 5.8a). With increasing Al content up to 44 at.%, the thickness of the oxide layer is reduced to about 0.298 p,m (Fig. 5.8b). Due to the incorporation of the oxygen, a porous structure is formed on the surface. As the Al content is further increased to 52 at.%, no visible oxide layer can be observed in the SEM cross-sections of the corresponding coating (Fig. 5.8c). This result indicates that the oxidation resistance of the $Y_{1-x}Al_xN$-coating can be effectively enhanced by incorporation of sufficient Al in the coating.

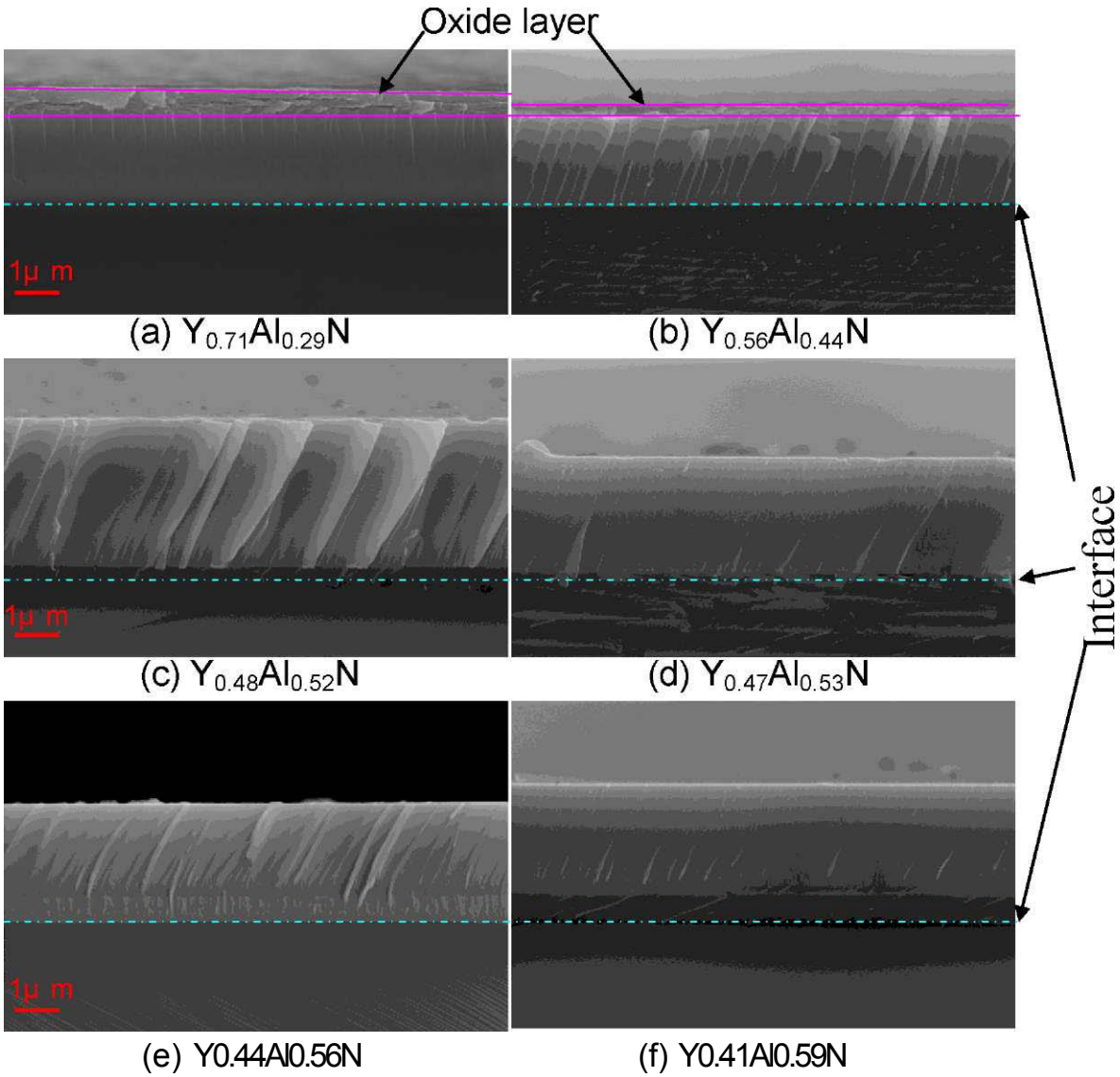

Fig. 5.8: SEM fracture cross-section of coatings as a function of the chemical composition after 5 weeks.

In order to clearly understand the development of the oxide scale on the $Y_{1-x}Al_xN$ coatings, SEM fracture cross-sections of the coating containing 29 at.% Al are shown in Fig. 5.9 after different exposure times a) after one day, b) after one week, c) after 5 weeks, respectively. The thickness of the oxide layer gradually increases as a function of exposure time. This result coincides with the previously discussed changes in the oxygen content (Table 5.3).

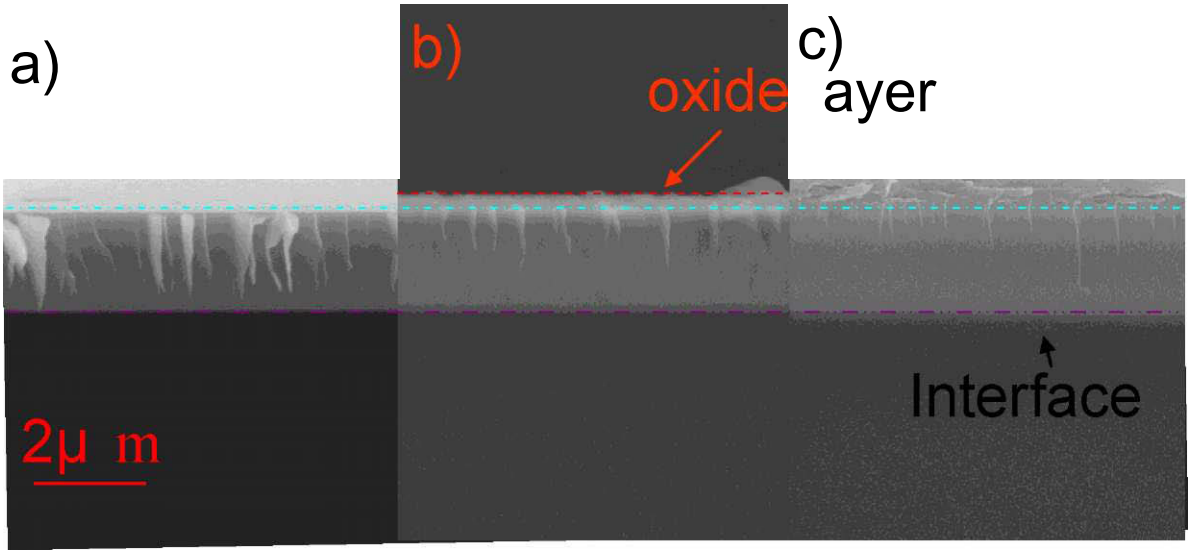

Fig. 5.9: SEM fracture cross-section of the $Y_{0.71}Al_{0.29}N$ coatings at different exposure times in ambient air: (a) after a day (b) after a week (c) after 5 weeks.

In order to determine the effect of oxidation time (exposure time) in ambient air, the coating oxide layer thickness were measured by Calo ® test (as shown in Fig. 5.10) and correlated to the information from the SEM fracture cross-sections for selected $Y_{1-x}Al_xN$ films.

The starting point of all lines refers to the as deposited state and indicates no oxide layer. The black curve refers to the coating with 29 at.% Al at the metallic sublattice, which rapidly oxidized after one day and forms a thick oxide layer. The ratio between the oxide layer and the total coating thickness (including the oxide layer) is expressed by t_o/t_t as a function of exposure time. For the lowest Al content of 29 at.% in the coating, the ratio increases from 0.090 to 0.125 to 0.129 to 0.222 with exposure times of 1,4,7 and 35 days, respectively. This indicates a continual increase of the oxide scale with time. For the coatings containing 44 and 52 at.% Al the oxide scale also steadily increases with time, although the extent of t_o/t_t is significantly reduced with increasing Al content. In contrast, the coatings containing >53 at.% Al seem to be unaffected by ambient air conditions. This indicates that 53 at.% Al can be regarded as a critical value for the formation of protective oxide layer in the $Y_{1-x}Al_xN$ films investigated.

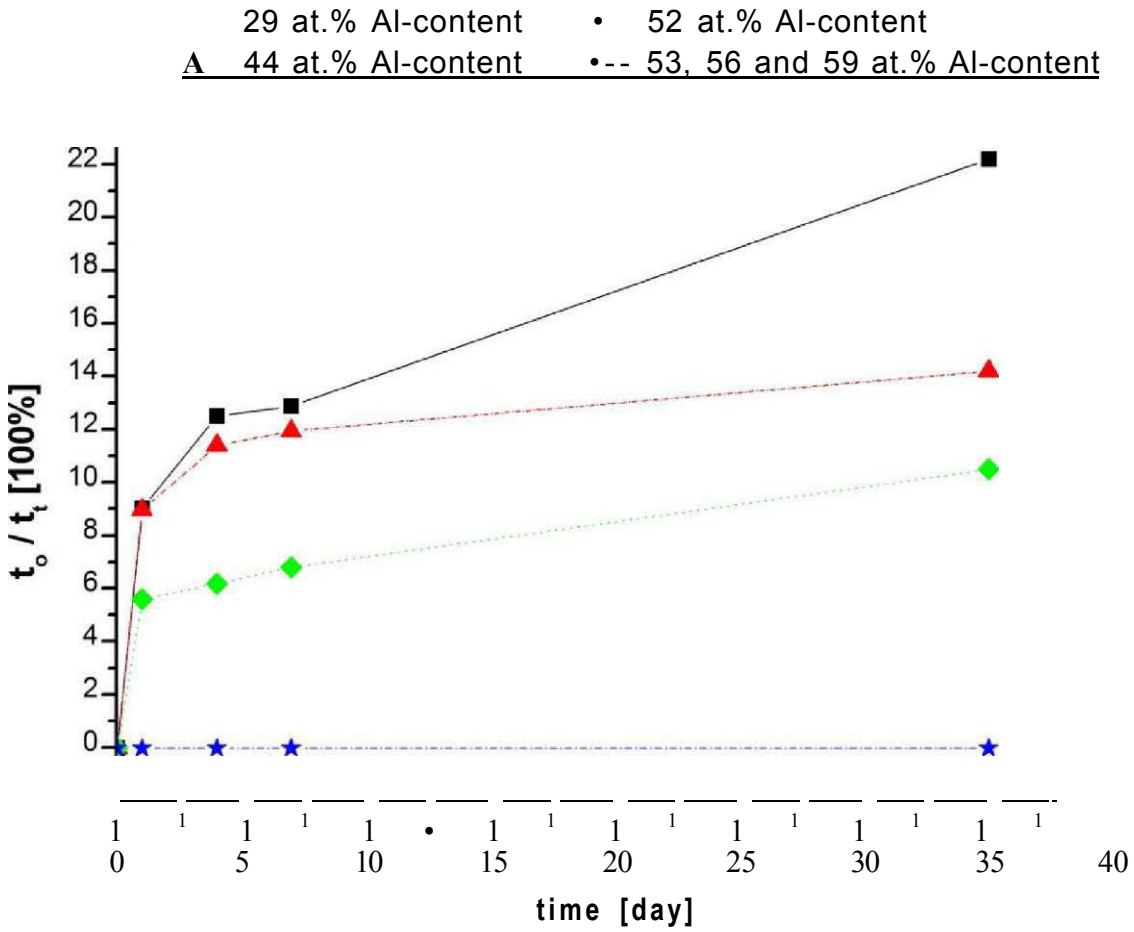

t_o: oxide layer thickness t_t: total coating thickness

Fig. 5.10: Ratio of the formed oxide layer and the total layer thickness (t_o/t_t) of $Y_{1-x}Al_xN$ coatings with different Al contents as a function of exposure time in ambient air.

Additionally, the color change of the $Y_{1-x}Al_xN$ coatings as a function of increasing Al content, can be seen in Fig. 5.11. The surface of the coatings containing 21-29 at.% Al is polychrome, whereas for the coating with Al contents between 44 and 52 at.%, a favored orange and green color can be observed. These colors disappear with a further increase in the Al content to > 52 at.% Al and change towards a purple/reddish color. Literature reports refer the room temperature oxidation of yttrium nitride crystals in air to this color development as a function of increasing oxide layer thickness [13], which is in good agreement to the above discussed oxide scale formation.

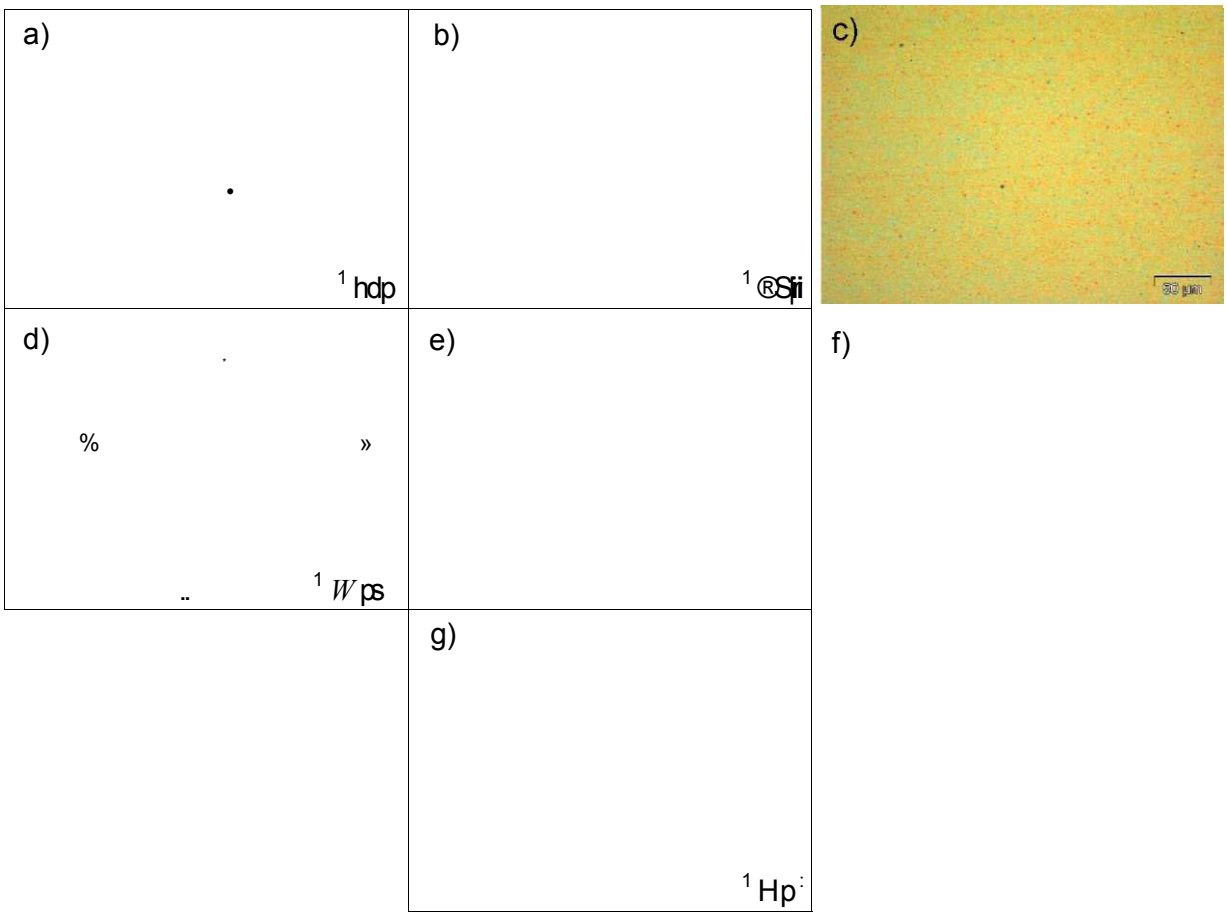

Fig. 5.11: The apparent color and the surface roughness of coatings change with increasing Al content (optical micrographs) after 2 months. a) 21 at.% Al b) 29 at.% Al c) 44 at.% Al d) 52 at.% Al e) 53 at.% Al f) 56 at.% Al g) 59 at.% Al.

5.2.1.3 Discussion

For a fixed temperature and constant pressure, the thermodynamic equilibrium is determined by a minimum of free enthalpy *G,* where

$$G = H - TS \qquad G = G_{min}\ (\mathrm{T},\ \mathrm{p} = \mathrm{const}) \tag{5.1}$$

H - Enthalpy, *S* - Entropy, *T* - Temperature, p - pressure [61].

Table 5.4 compares the formation enthalpies and entropies, as well as the Gibbs free energies of Y2O3 and Al2O3. It can be seen that the Gibbs free energy of a-AhO3 (-1581.9704 kJ/mol) and of Y-Al_2O_3 (-1562.724 kJ/mol) are lower than the Gibbs free energy for Y_2O_3 (-1816.6510 kJ/mol). This suggests, that the ambient oxygen more easily reacts with yttrium, creating a

Y_2O_3 oxide layer when the Al content is less than 53 at.%, compare Figs. 5.8 and 5.10. This rough estimation is in good agreement with the experimentally observed oxide scale formation on the $Y_{1-x}Al_xN$ coatings as the increasing incorporation of Al in the fcc-YN lattice by substitution of Y, obviously leads to the formation of mixed Al-Y-oxides for the low Al-containing coatings. Higher Al-contents in the coatings presumably result in the formation of dense stable aluminium oxides at the surface, protecting the underlying nitride form further oxidation. As the oxygen content in the coatings with $x < 53$ at.% rise with exposure time in ambient air it is clearly indicated that with reaching a threshold value of Al on the metallic sublattice, oxidation can effectively be reduced.

Table 5.4: Enthalpy of formation, entropy of formation and Gibbs free energy of Y_2O_3 and Al2O3 [80, 81].

Material	**Enthalpy of Formation**	**Entropy of Formation**	**Gibbs Free Energy**
	(kJ/mol)	**(J/K)**	**(kJ/mol)**
a-Al_2O_3	-1675.2736	50.91928	-1581.9704
Y-AhO3	-1656.864	59.8312	-1562.724
Y2O3	-1905.3099	99.07712	-1816.6510

5.2.2 Hf1-xAlxN - coatings

5.2.2.1 Chemical composition of the $Hf_{1-x}Al_xN$ - coatings

The $Hf_{1-x}Al_xN$ films were prepared by addition of aluminum platelets on the race track of powder-metallurgically produced targets with a Hf/Al ratio of 2.33 and 1.22, respectively. The chosen parameters, similar to the deposition of $Y_{1-x}Al_xN$ result in the formation of metastable coatings with chemical compositions summarized in Table 5.5. EDX investigations reveal that all Hf1-xAlxN films are overstochiometric in their nitrogen content, reaching values of N/(Hf+Al) from ~ 1.03 to 1.38. The manual Al-alloying resulted in Al-contents at the metallic sublattice from ~23 at.% to ~77 at.% by the number of increasing Al-platelets on the two different Hf-Al-targets, respectively. In contrast to the results from the $Y_{1-x}Al_xN$ films discussed above, no indication of oxygen can be found in the $Hf_{1-x}Al_xN$ films, compare Table 5.5.

Table 5.5: Chemical composition of $Hf_{1-x}Al_xN$ - coatings.

Target at.%	Number of the Al-platelets	coating nomenclature	elemental composition at.%				Al/(Al+Hf) at.%	N/(Al+Hf) at.%-ratio
			Hf	Al	Ar	N		
$Hf_{0.70}Al_{0.30}$	0	Hf0.77Al0.23N	35.01	10.52	-	54.47	23	1.196
	2	Hf0.67Al0.33N	29.93	15.02	-	55.06	33	1.225
	4	Hf0.60Al0.40N	27.41	18.49	3.15	50.95	40	1.11
	8	Hf0.43Al0.57N	17.37	23.49	2.89	56.24	57	1.376
	12	Hf0.38Al0.62N	17.85	28.73	2.94	50.48	62	1.084
Hf0.55Al0.45	0	Hf0.62Al0.38N	28.90	17.98	2.07	51.05	38	1.089
	8	Hf0.37Al0.63N	16.65	28.62	2.72	52.01	63	1.158
	12	Hf0.29Al0.71N	13.10	31.82	2.28	52.80	71	1.175
	16	Hf0.23Al0.77N	10.98	37.47	1.71	49.84	77	1.029

5.2.2.2 Phase composition (XRD)

The XRD pattern of the $Hf_{1-x}Al_xN$ coatings are shown as a function of Al content from bottom to top in Fig. 5.12. According to JCPDS standards, the peaks of the coatings containing 23 and 33 at.% Al (appearing at a 29 angle of ~ 39.58 ° (200) and 55.22° (220)) exhibit a single phase cubic structure of fcc-$Hf_{1-x}Al_xN$. At the same time, from the peak at 29 ~34.1 ° small fractions of hexagonal (wurtzite) phase can be detected. That means, a further increase of the Al-content from 23 at.% to 33 at.% results in a dual phase structure of fcc-$Hf_{1-x}Al_xN$ and wur-$Hf_{1-x}Al_xN$. An Al content of > 38 at.% leads to diminishing cubic (200) and (220) reflexes indicating that Al-contents above 38% favor a wurtzite phase dominated $Hf_{1-x}Al_xN$ structure. With increasing the Al content from 38 to 77 at.% the peak at 29 ~ 32.87 ° shifts to higher 29 angles. In other words, an incorporation of Al result in a decrease of the wur-Hf-Al-N lattice constants. This result may be caused by an incorporation of Al with smaller atomic radius than Hf into the hexagonal lattice. Literature reports using a band parameter approach, predict the transition from fcc-$Hf_{1-x}Al_xN$ to wur-$Hf_{1-x}Al_xN$ in the range of ~21.2 at.% Al at the metallic sublattice [59]. This result is in good agreement with the experimentally observed values discussed above.

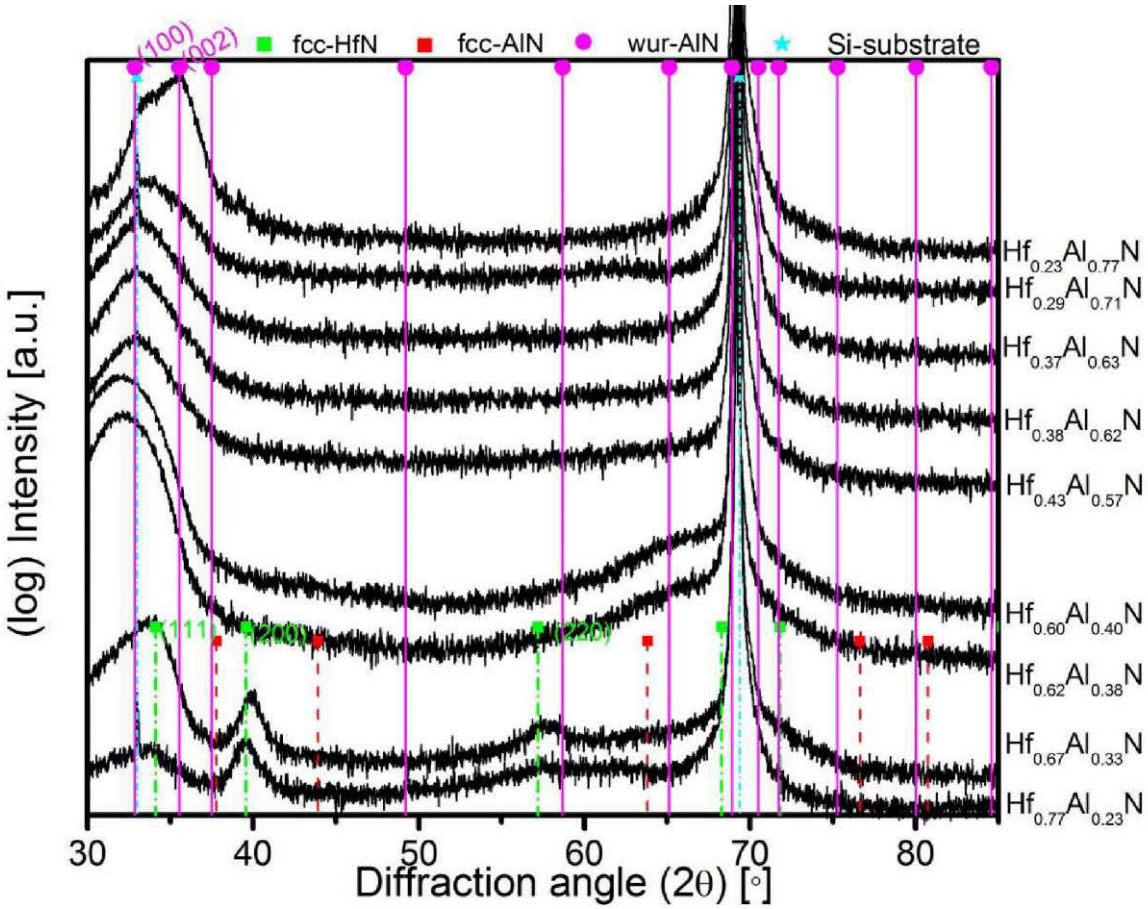

Fig. 5.12: XRD-pattern of the $Hf_{1-x}Al_xN$ coatings as a function of Al/(Hf+Al) atomic ratio.

5.2.2.3 Mechanical properties of $Hfi_{-x}Al_xN$ coatings

The hardness and Young's modulus of the $Hf_{1-x}Al_xN$ coatings with increasing Al content from 23 at.% to 77 at.% were measured by nanoindentation, as shown in Fig. 5.13. The hardness of these coatings decreases from 25.21 GPa to 23.98 GPa, when the Al content is raised from 23 at.% to 33 at.%, consistent with the formation of a dual phase structure of fcc-$Hf_{1-x}Al_xN$ and wur-$Hf_{1-x}Al_xN$. A further increase of the Al content from 38 to 63 at.% at the metallic sublattice results in a relatively low hardness of ~ 20 GPa. The more pronounced crystallinity of the films with Al content > 71 at.% (single phase wurtzite regime see Fig. 5.12) induces a slight H-increase. The reduction in Hardness and E-modulus is strongly correlated to the structure transition from single phase cubic over a mixed dual phase of fcc-$Hf_{1-x}Al_xN$ and wur-$Hf_{1-x}Al_xN$ into a single phase structure of wur-$Hf_{1-x}Al_xN$. This result can be explained by the lower mechanical properties and elastic constants of the hexagonal phase as compared to the cubic phase [82].

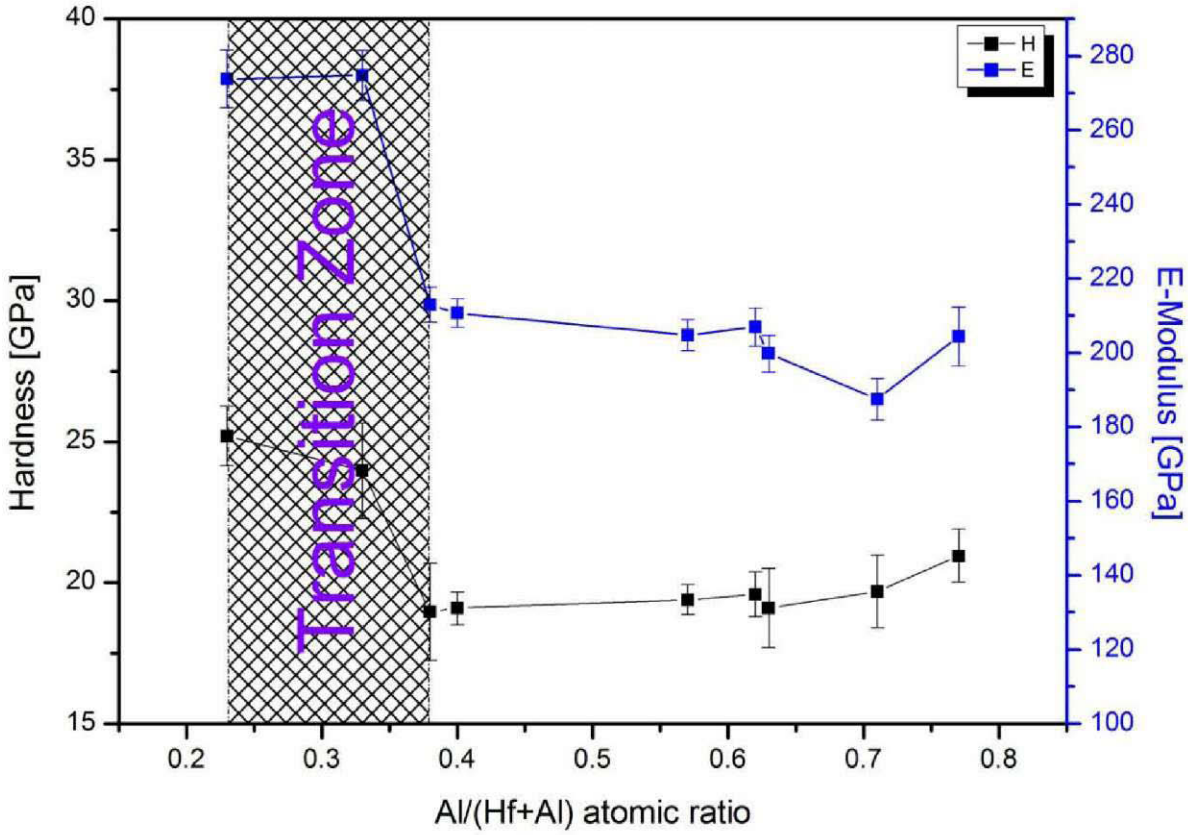

Fig. 5.13: Hardness and Young's modulus of the $Hf_{1-x}Al_xN$ coatings as a function of Al/(Hf+Al) atomic ratio.

5.2.2.4 Growth rate of $Hfi_{-x}Al_xN$ coatings

Growth rates of the $Hf_{1-x}Al_xN$ coatings as a function of the Al content are shown in Fig. 5.14, which were calculated from the coating thickness, using Calo®-test and the corresponding deposition time. Fig. 5.14 shows that the growth rate of the $Hf_{1-x}Al_xN$ coatings increases from 0.0573 p,m/min for a dual phase of fcc-$Hf_{1-x}Al_xN$ and wur-$Hf_{1-x}Al_xN$ to 0.113 p,m/min for a single phase of wur-$Hf_{1-x}Al_xN$ with increasing Al content from 23 at.% to 77 at.%, respectively. The increase in growth rate is caused by an increasing hexagonal phase fraction with increasing Al content, since the unit cell volume of the wurtzite phase V_h is ~ 26% larger as compared to the cubic volume [83].

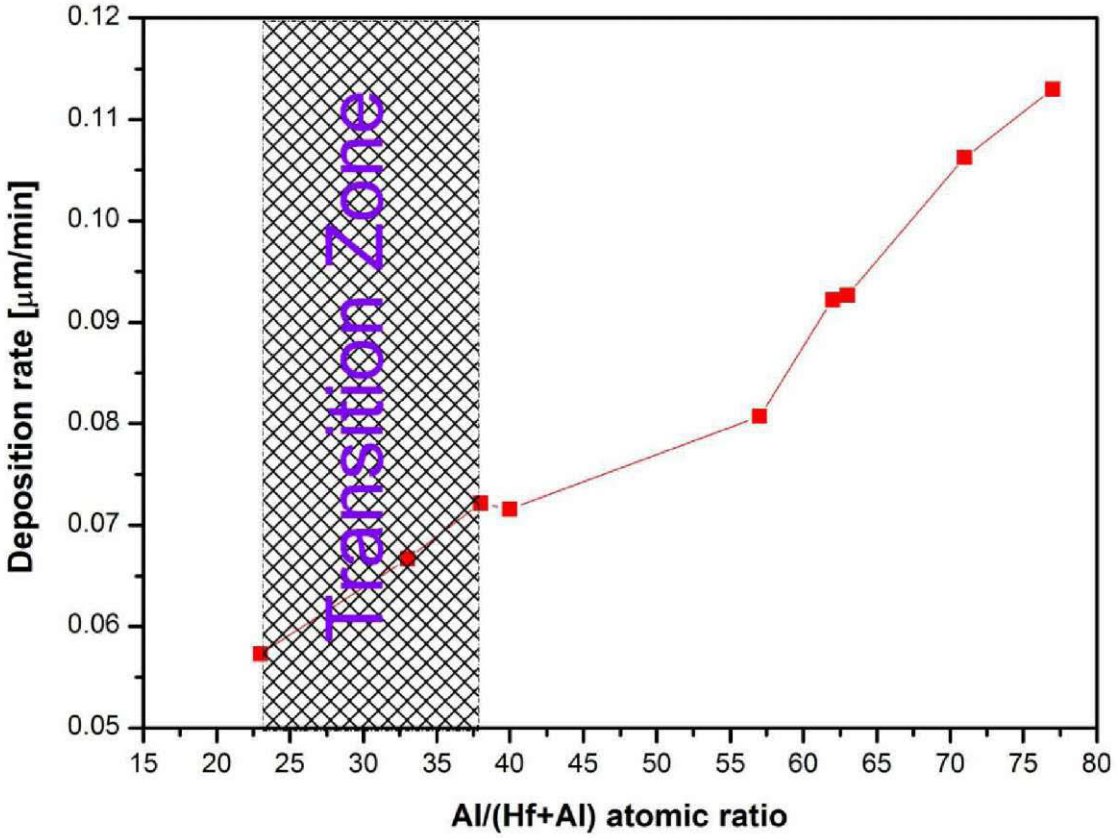

Fig. 5.14: Growth rate of the $Hf_{1-x}Al_xN$ coatings as a function of the Al content.

6 Summary and conclusion

In order to investigate the influence of Al addition on the microstructure and mechanical properties of YN_z and HfN_z, binary YN_z and ternary $Y_{1-x}Al_xN$ and $Hf_{1-x}Al_xN$ coatings were deposited on silicon substrate by unbalanced magnetron sputtering. N_2 as reactive gas and Ar as working gas were mixed at different N_2 partial pressures (P_{N2}/P_T) in order to examine the phase formation of YN_z. As the single phase YN_z films severely suffer from oxidation immediately after deposition, the fcc-YN_z was alloyed with Al to obtain a ternary $Y_{1-x}Al_xN$ compound. In addition, powder metallurgically produced $Hf_{1-x}Al_x$ targets with x = 0.3 and 0.45, were used for the reactive deposition of $Hf_{1-x}Al_xN$ by unbalanced magnetron sputtering.

The prepared YNz coatings were investigated by means of X-ray diffraction (XRD) and optical microscopy. Ranging P_{N2}/P_T from 0 to 10% results in the formation of a mixed phase structure of metallic Y, base-centered monoclinic-Y_2O_3 and body-centered cubic-Y_2O_3. By increasing P_{N2}/P_T up to 20% the fcc-YN phase begins to form with a preferred (200) orientation and with a small amount of both Y_2O_3 phases. A further increase of P_{N2}/P_T up to 40% causes that both base-centered monoclinic-Y_2O_3 and body-centered cubic-Y_2O_3 phase completely disappeared and a preferred (111) orientation develops. At the same time, the (111) peak shifts towards smaller angles with increasing P_{N2}/P_T. Therefore, this result leads to an increase of the lattice parameter from 4.875 A for P_{N2}/P_T = 20% to 4.968 A for P_{N2}/P_T = 70%. With increasing exposure time in ambient air, the oxide scale increases until spallation from the oxide scale occurs.

Furthermore, in order to improve the oxidation resistance of the fcc-YN coating (P_{N2}/P_T = 40%), alloying with 29, 44, 52, 53, 56 and 59 at.% Al was used to produce Y1-$_xAl_xN$ thin films. With increasing Al content to 52 at.% no visible oxide scale formation after deposition can be observed in the SEM cross-sections of the corresponding coating. In the Al-range from 29 at.% to 44 at.%, the thickness of the oxide scale increases with increasing time. The unoxidized part of the single phase c-$Y_{1-x}Al_xN$ coating with 29 at.% Al exhibits a dense columnar structure with a growth direction perpendicular to the substrate surface. The growth direction is slightly tilted with respect to the substrate normal due to the formation of the w-$Y_{1-x}Al_xN$ phase for > 44 at.% Al. The transition zone to the single-phase wurtzite structure is in the range from 37 at.% to 44 at.% Al content exhibiting a dual phase structure of fcc-$Y_{1-x}Al_xN$ and wur-Y1-$_xAl_xN$.

The fcc-HfN alloyed with Al content increasing from 23 at.% to 77 at.% formed a ternary solid solution of $Hf_{1-x}Al_xN$. Due to Al content above the solid solution limit, the hardness values of the corresponding coatings measured by nanoindentation decrease from 25.21 GPa to 23.98 GPa for 23 at.% and 33 at.% Al content, consistent with the formation of a dual phase structure of fcc-$Hf_{1-x}Al_xN$ and wur-$Hf_{1-x}Al_xN$. A further increase of Al content from 38 at.% to 63 at.% results in a wur-$Hf_{1-x}Al_xN$ dominated structure. As a result, the hardness values of these coatings decrease to ~ 20 GPa. In addition, the more pronounced crystallinity of the films with Al content > 71 at.% (single phase wurtzite regime) induces a slight hardness increase. A transition of the $Hf_{1-x}Al_xN$ coatings from a single phase cubic structure to a mixed dual phase of fcc-$Hf_{1-x}Al_xN$ and wur-$Hf_{1-x}Al_xN$ already begins for Al contents of less than 23 at.%.

In summary, the YN_z films present a single fcc structure with increasing N_2 partial pressure. However, the fcc-YN coatings easily oxidize in ambient air. By incorporation of Al into fcc-YN lattice with higher contents can be effectively prohibited. Furthermore, the higher Al contents promote the formation of the wurtzite phase of $Hf_{1-x}Al_xN$, at the same time, decreased hardness and Young's modulus values were obtained.

7 References

1. W. Gissler, H.A. Jehn, *Advanced Techniques for Surface Engineering,* Kluwer Academic Publishers, Italy, 1992.

2. J.R. Davis, *Surface Engineering for Corrosion and Wear Resistance,* ASM International, United States of America, 2001.

3. K. Wasa, M. Kitabatake, *H. Adachi, Thin Films Materials Technology: Sputtering of Compound Materials,* William Andrew, Inc., Norwich, 2004.

4. B. Alling, A. Karimi, I.A. Abrikosov, *Electronic origin of the isostructural decomposition in cubic $Mi_{-x}Al_xN$ (M=Ti, Cr, Sc, Hf): A first-principles study,* Surface and Coatings Technology, 203 (2008) 883-886.

5. B. Howe, J. Bareno, M. Sardela, J.G. Wen, J.E. Greene, L. Hultman, A.A. Voevodin,I. Petrov, *Growth and physical properties of epitaxial metastable $Hf_{1-x}Al_xN$ alloys deposited on MgO(001) by ultrahigh vacuum reactive magnetron sputtering,* Surface and Coatings Technology, 202 (2007) 809-814.

6. J.M. Castanho, M.T. Vieira, *Effect of ductile layers in mechanical behavior of TiAlN thin coatings,* Journal of Materials Processing Technology, 143-144 (2003) 352-357.

7. P.H. Mayrhofer, C. Mitterer, L. Hultman, H. Clemens, *Microstructural design of hard coatings,* Progress in Materials Science, 51 (2006) 1032-1114.

8. P.H. Mayrhofer, A. Horling, L. Karlsson, J. Sjolen, T. Larsson, C. Mitterer, L. Hultman, *Self-organized nanostructures in the Ti-Al-N system,* Applied Physics Letters, 83/10 (2003) 2049.

9. K. Kutschej, P.H. Mayrhofer, M. Kathrein, P. Polcik, R. Tessadri, C. Mitterer, *Structure, mechanical and tribological properties of sputtered $Ti_{1-x}Al_xN$ coatings with $0.5<x<0.75$,* Surface and Coatings Technology, 200 (2005) 2358-2365.

10. F. Vaz, L. Rebouta. M. Andritschky, M.F. da Silva, J.C. Soares, *Thermal oxidation of $Ti_{1-x}Al_xN$ coatings in air,* Journal of the European Creamic Society, 17 (1997) 1971-1977.

11. P.H. Mayrhofer, F.D. Fischer, H.J. Bohm, C. Mitterer, J.M. Schneider, *Energetic balance and kinetics for the decomposition of supersaturated $Ti_{1-x}Al_xN$,* Acta Materialia, 55 (2007) 1441-1446.

12. L. Mancera, J.A. Rodriguez, N. Takeuchi, *First principles calculations of the ground state properties and structural phase transformation in YN,* Journal of Physics: Condensed Matter, 15 (2003) 2625-2633.

13. L. Du, J.H. Edgar, R.A. Peascoe-Meisner, Y.Y. Gong, S. Bakalova, M. Kuball, *Sublimation crystal growth of yttrium nitride,* Journal of Crystal Growth, 312 (2010) 2896-2903.

14. D.L. Smith, *Thin-film deposition: principles and practice,* McGraw-Hill Professional, America, 1995.

15. D.M. Mattox, *Handbook of physical vapour deposition (PVD) processing: film formation, adhesion, surface preparation and contamination control, Materials Science and Process Technology Series,* William Andrew, America, 1998.

16. F.W. Bach, A. Laarmann, T. Wenz, *Modern Surface Technology,* WILEY-VCH Verlag GmbH and Co.KgaA, Weinheim, 2006.

17. M. Pfeiler, Diploma Thesis, *The influence of deposition temperature on $Ti_{1-x}Al_xN$ coated heat resistant high speed steels,* Leoben, 2005.

18. R.F. Bunshah, *Handbook of deposition technologies for films and coating: science, technology, and applications,* Noyes publications, America, 1994.

19. J.S. Brunell-Gray, P.K. Datta, *Surface Engineering Casebook,* Woodhead Publishing Ltd., Cambridge, 1996.

20. L.F. Chi, *Nanotechnology: Volume 8: Nanostructured Surfaces,* WILEY-VCH Verlag GmbH and Co.KgaA, Weinheim, 2010.

21. S. Baeumer, *Handbook of plastic optics,* WILEY-VCH Verlag GmbH and Co.KgaA, Weinheim, 2010.

22. G.Z. Cao, *Nanostructure and nanomaterials: synthesis, properties and applications,* Imperial College Press, London, 2004.

23. J.R. Davis, *Handbook of thermal spray technology,* ASM International, America, 2004.

24. G.S. May, C.J. Spanos, *Fundamentals of semiconductor manufacturing and process control,* John Wiley and Sons, New Jersey, 2006.

25. S. Franssila, *Introduction to microfabrication,* John Wiley and Sons, United Kingdom, 2004.

26. A.Z. Moshfegh, H.V. Kaenel, S.C. Kashyap, M. Wuttig, *Proceeding of the International Workshop on Physics and Technology of Thin films,* World Scientific Publishing CO. Pte. Ltd, Singapore, 2004.

27. H.O. Pierson, *Handbook of chemical vapour deposition (CVD): Principles, Technology, and Applications,* Noyes Publications, America, 1992.

28. J.L. Vossen, W. Kern, *Thin film processes II,* Academic Press, San Diego, 1991.

29. S.M. Rossnagel, J.J. Cuomo, W.D. Westwood, *Handbook of plasma processing technology: Fundamentals, Etching, Deposition, and Surface Interactions,* Noyes Publications, America, 1990.

30. M. Aliofkhazraei, A.S. RRouhaghdam, *Fabrication of Nanostructures by Plasma Electrolysis,* WILEY-VCH Verlag GmbH and Co.KgaA, Weinheim, 2010.

31. J.M. Proud, *Plasma processing of materials,* National Academy Press, Washington, 1991.

32. M. Konuma, *Film Deposition by Plasma Techniques,* Springer Verlag, 1992.

33. M. Ohring, *The materials science of thin films,* Academic Press, San Diego, California, 1991.

34. H.K. Pulker, *Coating on glass,* Elsevier Science B.V., Amsterdam, 1999.

35. B.M. Caruta, *Thin film and coating: new research,* Nova Science Publishers, Inc, New York, 2005.

36. J.E. Mahan, *Physical vapour deposition of thin film,* Wiley, 2002.

37. K. Wasa, S. Hayakawa, *Handbook of sputter deposition technology: principles, technology, and applications,* Noyes Publications, America, 1992.

38. T.M. Adams, R.A. Layton, *Introductory MEMS: Fabrication and Applications,* Springer Science+Business Media, New York, 2010.

39. R. Brown, *RF/Microwave Hybrids: Basics, Materials and Processes,* Kluwer Academic Publishers, Boston/Dordrecht/London, 2003.

40. K. Seshan, *Handbook of thin-film deposition processes and techniques,* Noyes Publications, 1988.

41. A. Paoletti, A. Tucciarone, *The physics of diamond,* Proprieta Letteraria Riservata, Italy, 1997.

42. K. Friedrich, A.K. Schlarb, *Tribology of polymeric nanocomposites,* Elsevier Publications, Great Britain, 2008.

43. C.A. Bishop, *Vacuum deposition onto webs, films, and foils,* William Andrew Publishing, America, 2006.

44. P.H. Mayrhofer, PhD-Thesis, *Materials science aspects of nanocrystalline PVD hard coating,* University of Leoben, 2001.

45. H. Frey, *Plasma Chemistry,* Cambridge International Science Publishing, Cambridge 1998.

46. W. Gissler, H.A. Jehn, *Advanced techniques for surface engineering,* Kluwer Academic Publishers, Brussels and Luxembourg, 1992.

47. J.W. Dini, *Electrodeposition: the materials science of coatings and substrates,* Noyes Publications, America, 1993.

48. J.A. Thornton, *High rate thick film growth,* Annual Review of Material Science, 7 (1977) 239.

49. P.B. Barna, M. Adamik, *Fundamental structure forming phenomena of polycrystalline films and the structure zone models,* Thin solid films 317 (1998) 27-33.

50. X.T. Yan, Y.D. Xu, *Chemical Vapor Deposition: An integrated engineering design for advanced materials,* Springer Verlag, London, 2010.

51. P.B. Barna, M. Adamik, *Fundamental structure forming phenomena of polycrystalline films and the structure zone models,* Thin Solid Films, 317 (1998) 27 - 33.

52. I. Petrov, P.B. Barna, L. Hultman, J.E. Greene, *Microstructural evolution during film growth,* Journal of Vacuum Science and Technology. 21(5) (2003) 117 - 128.

53. P.B. Barna, M. Adamik, in Y. Pauleau, P.B. Barna (Eds.), *Protective Coatings and Thin Films, Synthesis, Characterization and Applications,* Kluwer Academic Publishers, Dordrecht, 1997.

54. R.F. Bunshah, *Handbook of hard coatings: deposition technologies, properties and applications,* Noyes publications, America, 2001.

55. Wikipedia Contributors, *Yttrium nitride,* from Wikipedia, the free encyclopedia. http://en.wikipedia.org/wiki/Yttrium_nitride, 8 June 2010.

56. T. Bohnen, G.R. Yazdi, R. Yakimova, G.W.G. van Dreumel, P.R. Hageman, E. Vlieg, R.E. Algra, M.A. Verheijen, J.H. Edgar, *ScAlN nanowires: A cathodoluminescence study*, Journal of Crystal Growth, 311 (2009) 3147-3151.

57. http://www.springermaterials.com/docs/pdf/10522884_2145.html.

58. http://www.springermaterials.com/docs/pdf/10501684_1584.html.

59. Y. Makino, *Prediction of phase change in pseudobinary transition metal aluminum nitrides by band parameters method,* Surface and Coatings Technology, 193 (2005) 185-191.

60. S. PalDey. S.C. Deevi, *A Structural Materials Propperties Microstructure and Processing,* Materials Science and Engineering, 342 (2003) 58.

61. A. Kimura, H. Hasegawa, K. Yamada, T. Suzuki, *Effects of Al content on hardness, lattice parameter and microstructure of* $Ti_{1-x}Al_xN$ *films,* Surface and Coatings Technology, 120-121 (1999) 438.

62. G. Gottstein, *Physikalische Grundlagen der Materialkunde,* Springer Verlag, Berlin, 2007.

63. Zehua Zhang, Diploma Thesis, *Impact of Al on structure and mechanical properties of NbNand TaN,* University of Leoben, 2010.

64. User Manual A400 VL, Leybold AG.

65. Operational Manual ACG-6B, ENI Company Ltd.

66. User Guide Leybold Vacuum, Leybold AG.

67. User Guide Tylan General R 7030/7031, Tylan General GmbH.

68. User Manual Duo 20, Pfeiffer Vacuum GmbH, 2002.

69. M. Moser, PhD Thesis, *Structural evolution of protective coatings for y-TiAl based alloys,* University of Leoben, Leoben, 2008.

70. W.H. Bragg, W.L. Bragg, *Proceedings of the Royal Society of London.* Series A, Containing Papers of a Mathematical and Physical Character, 88/605 (1913) 428.

71. H. Willmann, PhD Thesis, *Al-Cr-N thin film design for high temperature applications,* Department of Physical Metallurgy and Materials Testing, University of Leoben, Leoben, 2007.

72. B.E. Warren, *X-Ray Diffraction,* Dover Publications, New York, 1990.

73. K. Nitzsche, *Schicht messtechnik,* Vogel, Wurzburg, 1997.

74. C.B. Carter, M.G. Norton, *Ceramic Materials: Science and Engineering,* Springer Science and Business Media LLC, New York, 2007.

75. A.C. Fischer-Cripps, *Nanoindentation,* Springer Science and Business Media LLC, New York, 2006.

76. IBIS, Fischer-Cripps Laboratory.

77. W.C. Oliver, G.M. Pharr, *An improved technique for determining hardness and elastic modulus using load and displacement sensing indentation experments,* Journal of Materials Research, 7 (1992) 1564-1583.

78. S. Sepeur, Nanotechnology, Quensen Druck+Verlag GmbH and Co. KG, Germany, 2008.

79. M. Moser, P.H. Mayrhofer, L. Szekely, G. Safran, P.B. Barna, *Influence of bipolar pulsed DC magnetron sputtering on elemental composition and micro-structure of Ti-Al-Y-N thin films*, Surface and Coatings Technology, 203 (2008) 148-155.

80. Mr. Everett's web page, *Yttrium (Ill) oxide,* site designed and maintained by Mr. Everett, http://www.mrteverett.com/Chemistry/q_compounds.asp?CAS=1314-36-9, 10 March 2011.

81. Mr. Everett's web page, *Yttrium (III) oxide,* site designed and maintained by Mr. Everett, http://www.mrteverett.com/Chemistry/q_compounds.asp?CAS=1344-28-1 10 March 2011.

82. P.H. Mayrhofer, D. Music, J.M. Schneider, *Influence of the Al distribution on the structure, elastic properties, and phase stability of supersaturated* $Ti_{1-x}Al_xN$, *Journal of Applied Physics*, 100/9 (2006).

83. R. Rachbauer, Diploma Thesis, *Comparative microstructural investigations of Ti-Al-N thin films alloyed with Y and Nb,* Department of Physical Metallurgy and Materials Testing, University of Leoben, Leoben, 2008.